修　士　論　文

題　目　Broadband frequency entangled photon generation using silicon nitride ring cavities

指導教員　竹内　繁樹　教授

京都大学大学院工学研究科 電子工学専攻

氏 名　殷　政浩

令和2年2月1日

Broadband frequency entangled photon generation using silicon nitride ring cavities

Zhenghao Yin

Abstract

Frequency entangled photon source is widely required in various optical quantum technology, including but no limited to quantum teleportation, cluster state quantum computation and quantum metrology etc. In the recent decade, chip-scale entangled photon source has been developed in silicon platform. However, due to the intrinsic two-photon absorption and transparent band of silicon, the high-intensity and broadband frequency entangled photon pairs is not fully realized. Here, we report the platform of silicon nitride to generate the frequency entangled photon pairs using spontaneous four wave mixing and realize

Contents

Chapter 1

Introduction

The flying qubit—photon—featuring the advantages of long coherent time and multiple degrees of freedom (DoF), is a promising candidate in quantum computation and quantum communication. However, in the term of DoF, much of research up to now focuses on the photon polarization and path entanglement realization, very little attention has been paid to the role of frequency entanglement, which is continuous and infinite in hilbert space.

Furthermore, the previous research shows that frequency entangled photon pairs can be exploited not only in wavelength division multiplexing quantum key distribution [1] but also transferring quantum information in future quantum networks [2]. Besides, in recent applications of quantum metrology, quantum optical coherent tomography (QOCT), the broadband frequency entanglement [3] is also required.

1.1 Background

Compared with crystal experiments, a chip-scale photon source has the advantages of scalability and robustness. A conventional material candidate is silicon on insulator (SOI), since it is CMOS-compatible and supplied by a lot of wafer manufacturers. However, suffering from two photon absorption and stimulated Raman scattering, silicon is no able to generate broadband frequency conversion. Since that, silicon nitride, which is transparent from visible to near infrared range, is preferred to perform broadband frequency entanglement. A recent record is single pair from visible to telecom band [4].

1.2 Objective

In the platform of silicon nitride, we utilize the third-order optical nonlinearity and confine the light in the sub-micron scale—optical waveguides. To enhance the nonlinear interaction, we define the ring resonator and couple the light inside along with a bus waveguide. The broadband property is ensured by carefully optimizing the device geometry to achieve a broadband phase matching condition. All the photon pair generation events are detected by single photon detectors and verified by the coincident counting.

In this dissertation, the terms 'broadband photon pair' is used to describe that pairs are generated in different frequency pairs simultaneously and but entangled only in the single mode pair.

1.3 Outline

The following chapters are sequentially divided in different topics.

Chapter 2

Principal theory

The way how light travels in a chip-scale is remarkably different the way in free-space. In the sub-micron scale, the electromagnetic wave can only propagate in a fewer cycles due to the constraint of material boundaries. However, since atoms and molecules are much smaller, the refractive index is not changed, as well as the reflection, interference and diffraction.

Based on these facts, in order to perform quantum optics experiments *at the bottom*, first, we shall confine the light propagation in a specific waveguide. On the other hand, thanks to modern laser technology, nonlinear optics is involved and give birth to optical frequency conversion. To enhance these nonlinear optical phenomena, we adopt the cavity structure and achieve sizable control.

In this chapter, we briefly introduce the guided wave theory and then move the cavity structure, ring resonators. Next, the nonlinear optics, in particular third-order nonlinear processes, is discussed in the following section. Although the quantum nature of photon pair generation distinct from the classical theory, all the physics mentioned above are necessary to analyse our essential research object, the silicon nitride ring resonators.

2.1 Guided-wave optics

In an ideal optical waveguide, the core layer and the cladding layer are usually composed of two different materials, where the refractive index is larger in the core. As an analogue of optical fibers, only in the higher index region can the light propagate, and meanwhile dissipate in a wavelength scale in the lower index region.

Usually, we assume the core and the cladding layer are made of nonmagnetic (magnetic permeability $\mu = \mu_0$) and dielectric material (conductivity $\sigma = 0$). Furthermore, we neglect the nonlinear response of the polarization of electric field

($\mathbf{P} \simeq \varepsilon_0 \chi \mathbf{E}$).

Since the waveguide in numerous research objects, is deposited or sputtered using chemical or physical methods, the uneven density in the waveguide layer can not be negligible. Hence, the propagation equation derived from Maxwell's equation is

$$(\nabla_\perp^2 + k^2 n^2 - \beta^2)\mathbf{E} = -(\nabla_\perp + i\beta\hat{\mathbf{z}})(\mathbf{E}_\perp \cdot \nabla_\perp \ln n^2) \tag{2.1}$$

where $\perp$ denotes the transverse component, $\nabla_\perp^2 = \nabla_x^2 + \nabla_y^2$. And k, n, β are the wave vector in vacuum, refractive index and propagation constant, respectively. While, with the negligible film anisotripy, Equation 2.1 can be approximated into

$$(\nabla_\perp^2 + k^2 n^2 - \beta^2)\mathbf{E} = 0 \tag{2.2}$$

This is the normal Helmholtz equation, indicating the relation between propagation constant β and material refractive index, i.e. chromatic dispersion.

Next, the boundary conditions determining the solution to Eqn. 2.2, arise from the Maxwell's equations as well.

$$\begin{aligned} \hat{\mathbf{n}} \cdot (\mathbf{E}_a - \mathbf{E}_b) &= 0 \\ \hat{\mathbf{n}} \times (\mathbf{H}_a - \mathbf{H}_b) &= 0 \end{aligned}$$

which is the continuity condition of both electric and magnetic field at all dielectric material interfaces. Here, $\hat{\mathbf{n}}$ is the normal direction at the material boundary and the subscript a, b denote different regions.

2.1.1 Waveguide modes

In the case of channel waveguides, the index discontinuity from both vertical and horizontal sides can be decomposed into two sets of independent and complete conditions, i.e. the horizontal boundary condition and vertical boundary condition, with the discontinuity on the waveguide corners neglected. In other words, approximately the equation has two independent partiuclar solutions, which is the mathematical origin of transverse electric (TE) modes and transverse magnetic (TM) modes.

Hence, we can study the eigenequantion by selecting only one set of boundary condition, as used in the the effective index method. For example, in a planar waveguide shown in Figure 2.1 ,$\mathrm{d}^2/\mathrm{d}y^2 = 0$[1], the TE mode features $E_x = 0$ and consider only y-component,

$$\frac{\mathrm{d}^2 E_y}{\mathrm{d}x^2} + (k^2 n^2 - \beta^2)E_y = 0 \tag{2.3}$$

[1]Since the planar waveguide is infinite at the y-direction , thus the solution is identical in arbitrary xz-plane, which means no gradient along x-axis.

and E_y is continous at $x = \pm d/2$, where d is the thickness of core layer.

For the region $|x| > d/2$, the light evanesces at x-direction at rate κ and in contrast, in the region of core layer, the light performs like stationary wave, denoting with k_x. By substituting these conditions, phase continuity is achieved between two interface

$$2k_x d = m\pi + 2\arctan(\kappa/k_x) \tag{2.4}$$

where m is the index of stationary wave. The second term can be treated as the Goos-Hänchen phase shift. Overall, the waveguide modes characterize that the phase shall maintain itself with an $m\pi$ shift along with the shift at the boundaries.

In the case of TM modes, the eigen equation is

$$2k_x d = m\pi + 2\arctan(\delta\kappa/k_x) \tag{2.5}$$

where $\delta = n_a/n_b$ is the index ratio and only differs from Equation 2.4 with this parameter. conclusively, the less is δ parameter, the propagation constant of TE and TM modes are closer.

2.1.2 Dispersion relation

Based on Equation 2.4 and Equation 2.5, k_x can be solved and then utilized to calculate propagation constant β, since $n_a^2 k^2 = k_\perp^2 + \beta^2$. In the case of channel waveguides, the TE and TM solutions are both necessary. Therefore, propagation constants β can be expressed as the product of free space wave vector k and the effective index n_{eff}

$$\beta = n_{\text{eff}} k = n_{\text{eff}}(\lambda)\frac{2\pi}{\lambda} = n_{\text{eff}}(\omega)\frac{\omega}{c} \tag{2.6}$$

along with the differential form

$$\frac{\mathrm{d}\beta}{\mathrm{d}k} = n_{\text{eff}} + k\frac{\mathrm{d}n_{\text{eff}}}{\mathrm{d}k} = n_{\text{eff}} - \lambda\frac{\mathrm{d}n_{\text{eff}}}{\mathrm{d}\lambda} \equiv n_g \tag{2.7}$$

$$\frac{\mathrm{d}\omega}{\mathrm{d}\beta} = c\frac{\mathrm{d}k}{\mathrm{d}\beta} = \frac{c}{n_g} \equiv v_g \tag{2.8}$$

which defines the group index n_g and group velocity v_g.

This formula linking $\beta - k$ or $\beta - \omega$ is named as dispersion relation, which gives the physics that light with different color propagates at different *speed*. Furthermore, Equation 2.4 and Equation 2.5 also indicate that the dispersion relation intrinsically depends on waveguide geometry.

2.2 Ring resonators

The ring resonators comprise of a bus waveguide and a ring waveguide, are usually demonstrated as optical filters or modulators at a wide range of platforms. The working principle of ring resonator can be derived completely [5] as an analogue to Fabry-Pérot etalon, based on the coupling mode theory.

In the model illustrated in Figure 2.2, the self-coupling coefficient τ and the cross-coupling coefficient κ can be evaluated analytically or using numerical simulation. Assuming the coupling only occur at the very close area, τ, κ are the power splitting ratios of the coupler and satisfy $\tau^2 + \kappa^2 = 1$ if the coupling section is lossless. a is the single-pass amplitude transmission, including both propagation loss in the ring and loss in the couplers.

The transmission rate of a all-pass type ring cavity takes the form of

$$T = \frac{I_{\text{pass}}}{I_{\text{input}}} = \frac{a^2 - 2a\tau\cos\phi + \tau^2}{1 - 2ar\cos\phi + a^2\tau^2} \tag{2.9}$$

where $\phi = \beta L$ is the phase shift in a single round trip.

2.2.1 Coupling condition

By plotting the function in Figure 2.3, we can see, the extinction ratio of absorption peak is defined by the self-coupling coefficient τ and the single-pass amplitude transmission a due to device geometric differences, like the gap between the bus waveguide and the ring cavity. Namely, a and τ both determine the coupling condition, which can be categorized in three cases

- **weak coupling** $a > \tau$. The loss inside the ring is larger than the power coupled from bus waveguides.
- **critical coupling** $a = \tau$. The loss and self-coupling are in balance. The optical power restored in the resonator achieve the minimum.
- **over coupling or strong coupling** $a < \tau$. The coupling is too strong for the light to dissipate in a single round trip.

Previous work [6] proposed a method to evaluate the coupling condition above using the experimentally measured device transmission. Considering the loss in the coupler, bent segment of ring and higher mode perturbance, usually the critical coupling varies from modes and the cross section of waveguides [7].

2.2.2 Spectrum characteristics

Meanwhile, the minimum of transmission rate T can be achieved periodically as $\phi = 2m\pi$, which defines the resonance of ring resonators. Therefore, the resonance condition is derived as

$$\beta L = 2m\pi \tag{2.10}$$

where m is the mode index. Specifically, the propagation constant β, shall be an integral times of a quasi wave vector $2\pi/L$. With this condition, the free spectral range (FSR) of wavelength and frequency are obtained

$$\Delta\lambda_{\mathrm{FSR}} \approx \frac{\lambda_{\mathrm{res}}^2}{n_g L} \tag{2.11}$$

$$\Delta\omega_{\mathrm{FSR}} \approx \frac{2\pi c}{n_g L} \tag{2.12}$$

In both wavelength and frequency domain, FSR determines the spacing of neighbouring resonant peak. This is a significant factor when the ring resonators are designed.

Furthermore, from Equation 2.9, the full width at half maximum (FWHM) of the resonance spectrum is derived as $\delta\lambda$

$$\delta\phi = \frac{2(1 - a\tau)}{\sqrt{\tau a}} \tag{2.13}$$

Likely, since the phase ϕ is related with the wave vector k in Equation 2.7. Substituting $\delta\phi = L n_g \delta k$, the half width of wavelength is

$$\delta\lambda = \frac{\mathrm{d}\lambda}{\mathrm{d}k}\delta k = \frac{\lambda_{\mathrm{res}}^2}{2\pi L n_g}\frac{2(1 - a\tau)}{\sqrt{\tau a}} \tag{2.14}$$

the same, at the frequency domain

$$\delta\omega = \frac{\mathrm{d}\omega}{\mathrm{d}k}\delta k = \frac{c}{L n_g}\frac{2(1 - a\tau)}{\sqrt{\tau a}} \tag{2.15}$$

Note in Equation 2.11 Equation 2.12 Equation 2.14 and Equation 2.15, the group index n_g is explicit instead of the effective index n_{eff} because both free spectral range and full width depend on the differential form, Equation 2.7.

And the finesse F of the resonator is defined

$$F \equiv \frac{2\pi}{\delta\phi} = \frac{\pi\sqrt{\tau a}}{2(1 - a\tau)} \tag{2.16}$$

Finally, we define the quality factor, a measure of the sharpness of the resonance relative to its central frequency.

$$Q = \frac{\lambda_{\text{res}}}{\delta\lambda} = \frac{\pi L n_g \sqrt{\tau a}}{\lambda_{\text{res}}(1 - a\tau)} \tag{2.17}$$

Usually, the Q-factor can be decomposed into two parts by formula $Q^{-1} = Q_i^{-1} + Q_l^{-1}$. And Q_i, Q_l are intrinsic Q-factor and loaded Q-factor, referring to the loss inside the ring waveguide and at the coupler, respectively. The physical meaning of the finesse and Q-factor relates to the number of round-trips before being lost to internal loss and the bus waveguides when the power is depleted to $1/e$ of its initial value.

2.3 Thrid-order nonlinear optics

Although the nonlinear effect is ignored during the derivation of waveguide modes in Section 2.1, for numerous materials, the nonlinear response of electric field is significant even at mW level, which is easy to occur with assistance of modern lasers. The origin of nonlinear optic phenomena is similar to the movement of the object in a potential field, such as the ball-spring model.

In the nonlinear material, the atoms or molecules are driven by the external electric field, due to the around chemical bonds or molecular orientation, the displacement of atoms or molecules perform nonlinear dependence on the strength of field. In real-world materials, interaction coming arising from various frequency leads to the addition or subtraction of these frequency components. This explains the frequency conversion nature in nonlinear optics.

It is worth mentioning that not only in the bulk crystals, but also in the sub-micron scale [8], the nonlinear response is still efficient, even over a single-layer two-dimensional material.

Here, a brief theoretical derivation is elucidated and in the following part, degenerate four wave mixing is emphasized. In an isotropic nonlinear medium, assuming only instantaneous dielectric response, the relation between the polarization and the electric field is expressed by a power series in the electric field

$$\mathbf{P}(t) = \varepsilon_0(\chi^{(1)}\mathbf{E}(t) + \chi^{(2)}\mathbf{E}^2(t) + \chi^{(3)}\mathbf{E}^3(t)) \tag{2.18}$$

$$= \varepsilon_0\chi^{(1)}\mathbf{E}(t) + \mathbf{P}_{\text{NL}}(t) \tag{2.19}$$

Note in Equation 2.18, the nonlinear susceptibilities $\chi^{(2)}$ and $\chi^{(3)}$ are second-rank and third-rank tensors, corresponding to the tensor product with $\mathbf{E}^2$ and $\mathbf{E}^3$. The higher order response is neglected and sequentially, only $\chi^{(2)}$ processes and $\chi^{(3)}$ processes are to be introduced.

$\chi^{(2)}$ **processes**

In centrosymmetric crystals such as silicon, the second-order susceptibility term is absent. However, in other materials like lithium niobate ($LiNbO_3$) and aluminium nitride (AlN), the second-order nonlinearity are essential to realize electro-optic modulation and second harmonic generation.

$\chi^{(3)}$ **processes**

Silicon and silicon nitride are both cubic crystal. Due to the third-order dependence, another factor equivalent to the optical intensity is involved, the $\chi^{(3)}$ process is also named as intensity-dependent effect or Kerr effect.

Consider three frequency components of $\mathbf{E}^3$, using the complex expression of electric field

$$\mathbf{E}(\mathbf{r},t) = \sum_{k=1}^{3} \mathbf{E}_{\omega_k}(\mathbf{r},t) = \frac{1}{2}\sum_{k=1}^{3}\left(\mathbf{E}_{\omega_k}(\mathbf{r})e^{i\omega_k t} + c.c.\right) \tag{2.20}$$

Substituting into third-order term in Equation 2.18 and arranging with the same propagation direction, the third-order polarization is

$$\begin{aligned}
\mathbf{P}^{(3)}(t) = {} & \frac{3}{4}\varepsilon_0\chi^{(3)}\left[|\mathbf{E}_{\omega_1}|^2\mathbf{E}_{\omega_1} + \cdots\right] && \text{SPM} \quad (2.21)\\
& + \frac{6}{4}\varepsilon_0\chi^{(3)}\left[(|\mathbf{E}_{\omega_2}|^2 + |\mathbf{E}_{\omega_3}|^2)\mathbf{E}_{\omega_1} + \cdots\right] && \text{XPM} \quad (2.22)\\
& + \frac{1}{4}\varepsilon_0\chi^{(3)}\left[(\mathbf{E}_{\omega_1}^3 e^{i\omega_1 t} + c.c.) + \cdots\right] && \text{THG} \quad (2.23)\\
& + \frac{3}{4}\varepsilon_0\chi^{(3)}\left[\frac{1}{2}(\mathbf{E}_{\omega_1}^2\mathbf{E}_{\omega_2} e^{i(2\omega_1+\omega_2)t} + c.c.) + \cdots\right] && \text{FWM} \quad (2.24)\\
& + \frac{3}{4}\varepsilon_0\chi^{(3)}\left[\frac{1}{2}(\mathbf{E}_{\omega_1}^2\mathbf{E}_{\omega_2}^* e^{i(2\omega_1-\omega_2)t} + c.c.) + \cdots\right] && \text{FWM} \quad (2.25)\\
& + \frac{6}{4}\varepsilon_0\chi^{(3)}\left[\frac{1}{2}(\mathbf{E}_{\omega_1}\mathbf{E}_{\omega_2}\mathbf{E}_{\omega_3} e^{i(\omega_1+\omega_2+\omega_3)t} + c.c.) + \cdots\right] && \text{FWM} \quad (2.26)\\
& + \frac{6}{4}\varepsilon_0\chi^{(3)}\left[\frac{1}{2}(\mathbf{E}_{\omega_1}\mathbf{E}_{\omega_2}\mathbf{E}_{\omega_3}^* e^{i(\omega_1+\omega_2-\omega_3)t} + c.c.) + \cdots\right] && \text{FWM} \quad (2.27)
\end{aligned}$$

In above equations, $\cdots$ stands for all possible permutation terms contributed by frequencies $\omega_1, \omega_2, \omega_3$. The abbreviation on the right side represent for

SPM, self-phase modulation

SPM adds an intensity-dependent term except the linear polarization, leading to a broadening of the pulse spectrum.

Note the $\chi^{(3)}$ is complex, thus the imaginary part may contribute to another intensity-dependent absorption mechanics, which is usually depicted in the two-photon absorption (TPA). The free carriers excited by TPA in further change the temporally both the absorption coefficient and the refractive index of material.

$$n = n_0 + n_2 I + i\frac{\lambda}{4\pi}(\alpha_0 + \alpha_2 I) \tag{2.28}$$

where the I is the intensity, n_2 is the Kerr coefficient and α_0, α_2 are related with TPA-induced free carrier absorption (FCA) and free carrier index (FCI) change, both interrelated with third-order susceptibility

$$n_2 = \frac{1}{cn_0^2\varepsilon_0}\frac{3}{4}\,\mathrm{Re}\left\{\chi^{(3)}\right\} \tag{2.29}$$

$$\alpha_2 = \frac{-\omega}{c^2 n_0^2\varepsilon_0}\frac{3}{2}\,\mathrm{Im}\left\{\chi^{(3)}\right\} \tag{2.30}$$

A figure of merit (FOM) is often used to compare the magnitude of Kerr coefficient n_2 with the strength of the TPA coefficient α_2

$$\mathrm{FOM} = \frac{1}{\lambda}\frac{n_2}{\alpha_2} \tag{2.31}$$

XPM, cross-phase modulation

XPM can be seen the first signal index influenced by a second signal. And the coeffiecient of XPM is twice as strong as the SPM coefficient.

THG, third-harmonic generation

Like SHG, THG generated a new frequency with is one-third of input frequency.

FWM, four wave mixing

In FWM process, more than three frequencies are involved. Nevertheless, Equation 2.24 and Equation 2.25 contain two identical wave, sometime calles as degenerate four wave mixing (DFWM). And Equation 2.26 and Equation 2.27 is a truly four wave process. Similar to the relation between SPM and XPM, the non-degenerate FWM is naturally twice stronger.

Traditionally, following the terminology in laser field, in DFWM, the ω_1 square term Equation 2.25 is labeled as pump frequency, and another two frequencies are referred to signal and idler frequency.

Besides, the imaginary part of third-order susceptibility incorporate other four-wave absorption mechanics, such as stimulated Brillouin scatter (SBS) and stimulated Raman scattering (SRS), which originate from acoustic waves in crystals and vibrating molecules.

Finally, it worth mentioning that in all THG and FWM processes, different from SPM and XPM processes, phase matching condition is required due to the complex exponential factors. In this case, the phase mismatch can change the polarization rapidly and leads to periodical variation in these parametric processes.

Chapter 3

Phase match condition for spontaneous four wave mixing in a ring cavity

According to the previous chapter, in a typical nonlinear optical waveguide or silica fibers, despite the stimulated Raman and Brillouin scattering, the frequency conversion processes involve not only the self-phase modulation of pump light and cross-phase modulation of signal and idler light, but also the phase mismatch in four wave mixing propagation factor. In this case, it is necessary to study the coupled nonlinear equations involving signal, idler and pump intensity [9].

Whereas in ring resonators, whose mode linewidth (pm) is much narrower than self-phase modulation frequency broadening, the frequency broadening in single mode is negligible. Thus the phase mismatch among cavity modes becomes the critical factor of the band of four wave mixing.

This chapter first describes the major origin of phase mismatch, chromatic dispersion, and goes on to the design philosophy used in device fabrication. Besides, several topics concerning the band of phase matching are also included.

3.1 Chromatic dispersion

In a typical FWM process, both energy conservation and momentum conservation are required

$$\beta_i + \beta_s = 2\beta_p \tag{3.1}$$

$$\omega_i + \omega_s = 2\omega_p \tag{3.2}$$

where the subscripts s i p stand for signal, idler and pump light.

Meanwhile, the resonance condition Equation 2.10 leads to $\beta = m\frac{2\pi}{L}$. Thus, Equation 3.1 is equivalent to

$$m_i + m_s = 2m_p \tag{3.3}$$

We can see that *the momentum conservation agrees with mode number conservation.* That is to say, as pump light sets into resonant wavelengths, by choosing the equidistant modes relative to the pump mode, the momentum conservation can be naturally satisfied. This is the most important difference from non-resonant devices.

Therefore, we can estimate the phase mismatch only in the frequency domain. Expand the resonant frequency into Taylor seires at ω_0 to the propagation constant β

$$\begin{aligned} \omega_\mu &= \omega_0 + \sum_{j=1} \frac{\mathrm{d}^j\omega}{\mathrm{d}\beta^j}\frac{(\beta-\beta_0)^j}{j!} \\ &= \omega_0 + \sum_{j=1} \frac{\mathrm{d}^j\omega}{\mathrm{d}\beta^j}\left(\frac{2\pi}{L}\right)^j \frac{\mu^j}{j!} \\ &= \omega_0 + D_1\mu + \frac{D_2}{2!}\mu^2 + \frac{D_3}{3!}\mu^3 + \cdots \end{aligned} \tag{3.4}$$

where $D_j \equiv (\frac{2\pi}{L})^j \ \mathrm{d}^j\omega \big/ \mathrm{d}\beta^j$ are j-order mode number dispersion parameter, whose dimension are all T^{-1} and $\mu \in \mathbb{Z}$ is the relative mode number.

It is easy to know that $D_1/2\pi = v_g/L$ is the free spectral range in the frequency and indicates that the dispersion property is related with the difference of resonant frequencies.

Next, we introduce the integrated dispersion D_{int} [10] to analyze the phase mismatch

$$\begin{aligned} D_{\mathrm{int}}(\mu) &\equiv \omega_\mu - (\omega_0 + D_1\mu) \\ &= \frac{D_2}{2!}\mu^2 + \frac{D_3}{3!}\mu^3 + \cdots \end{aligned} \tag{3.5}$$

In particular, D_{int} is the residual dispersion higher than second order. Approximately, if $D_3\mu \ll D_2$, the second-order dispersion will dominate the integrated dispersion both at signal and idler mode.

Indeed, the mode number dispersion parameter is linked with the dispersion coefficients in frequency and wavelength domain, giving such a chain rule

$$D_2 = -\frac{L}{2\pi}D_1^3\beta_2 = \frac{L}{2\pi}\frac{\lambda^2}{2\pi c}D_1^3 D_\lambda \tag{3.6}$$

where $\beta_2 = \mathrm{d}^2\beta / \mathrm{d}\omega^2$ is group velocity dispersion (GVD) and $D_\lambda = -(\lambda/c)\ \mathrm{d}^2 n / \mathrm{d}\lambda^2$ is the dispersion parameter.

In this method, we can analyze the phase mismatch in FWM quantitatively

$$\begin{aligned}\Delta\omega &\equiv \omega_s + \omega_i - 2\omega_p \\ &= D_{\mathrm{int}}(\mu) + D_{\mathrm{int}}(-\mu) \\ &= 2\left(\frac{D_2\mu^2}{2!} + \frac{D_4\mu^4}{4!} + \frac{D_6\mu^6}{6!} + \cdots\right)\end{aligned} \tag{3.7}$$

From the above derivation, the frequency mismatch $\Delta\omega$ only adds to the even terms of Taylor series in Equation 3.4. To conclude, a rough presupposition to increase the efficient phase matched band is achieving zero and flat dispersion around pump wavelengths.

3.2 Dispersion compensation

Previously mentioned in Section 2.1, the dispersion behaviour in integrated devices is not only the intrinsic material property, but also depends on the waveguide dimension.

In other words, the phase mismatch occurs as a result of material dispersion D_M and waveguide dispersion D_W, $D_\lambda = D_M + D_W$. Here, we adopt the wavelength dispersion parameter since the wavelength domain is measurable.

Usually, the Sellmeier equation is used to fit the refractive index for a particular transparent medium based on the Lorentz-Drude mode. Luke *et al.* reported the below measured refractive index of stoichiometric Si_3N_4 film [11]

$$n^2_{\mathrm{Si_3N_4}} = 1 + \frac{3.0249\lambda^2}{\lambda^2 - 135.3406^2} + \frac{40314\lambda^2}{\lambda^2 - 1239842^2} \tag{3.8}$$

This Sellmeier equation is valid over the wavelength range 310–5504 nm. The result of Equation 3.8 is plotted in Figure 3.1, along with the material dispersion parameter D_M, which is calculated at the precision of nm using the second-order finite difference of refractive index. In the telecom C-band, n=1.9963 and D_M = -6.57 ps/(km nm), which suggests the material dispersion at this range is considerably small.

On the other hand, the numerical simulation is adopted to evaluate the waveguide parameter. We use commercial software nmLumerical MODE to solve for the refractive index of fundamental TE modes. Shown in Figure 3.2, the dimension dependence of waveguide dispersion features negative values in the small waveguide size, i.e. behaving as normal dispersion at the second order. Nevertheless, as either the thickness or width of channel waveguide increases, D_W turns positive.

This indicates that to achieve zero dispersion in phase match condition of four wave mixing, the normal material dispersion can be compensated with anomalous waveguide dispersion.

For example, at 1550 nm, in a 1.5-µm-wide and 0.8-µm-thick silicon nitride waveguide cladded by silica, where the refractive index is 1.48, the waveguide dispersion is 122.56 ps/(km nm). Substituting into the second-order dispersion chain rule in Equation 3.6, the second-order mode number dispersion parameter D_2 is about 3.07 MHz. It is close to zero dispersion for the pump wavelength.

3.3 Dispersion engineering using slot structure

The slot waveguide was firstly realized by Xu *et al.* experimentally [12]. The same group, Almeida *et al.* then discussed the light enhancement and confinement caused by large discontinuity of the electric field at high-index-contrast interfaces [13]. In the recent decade, it is fully studied that such a novel waveguide can be also used to design dispersion-flattened waveguide [14–17], including the both vertical or horizontal and single or multiple slots. It is also reported a micro-ring resonators formed by a slot hybrid waveguide exhibits a flat and low anomalous dispersion [18].

In our research, the vertical slot is preferred due to the easy fabrication during the monolithic process. For example, in a double vertical slot waveguide illustrated in Figure 3.3, two extra gaps are fully etched and then reburied with low-index medium instead. Except the waveguide width w and thickness t, two extra parameters are defined, the position factor pf, ratio of slot position to the waveguide width w, and the filling factor ff, ratio of slot width to the waveguide width.

To classify the modes in this slot structure, the same mode solver mention in previous section is performed. In the result shown in Figure 3.4, in TM0 and TM1 modes, the light is confined strongly in the slots while the TE0 and TE1 is similar to the normal TE modes, where the discontinuity is obvious on the upper and lower interfaces.

Furthermore, by optimizing the position and filling factors, the near-zero and flattened dispersion can be obtained.

3.4 Effects of mode crossing

In the conclusion of Section 3.2, only in the wider or thicker waveguides can the zero dispersion be compensated. However, despite the fabrication difficulty arising from thicker films, the waveguide of larger size also supports high order modes.

In this case, due to the perturbation of high order modes, the linear mode coupling occurs and influences the resonance spectrum. In the study of soliton generation, it is found that avoided mode crossings induced by linear mode coupling can prevent optical soliton formation when affecting resonator modes close to the pump laser frequency [19, 20]. On the other hand, by introducing artificial mode crossing, the anomalous group velocity can also be achieved [21]. Even though the phenomena mentioned in these works are classical, but in the term of phase matching condition, the physics is similar.

In the following research, the mode crossings found in our devices not only change the spectrum transmission, but also leads to failure of evaluating the dispersion properties.

Chapter 4

Device fabrication of silicon nitride ring resonators

Different from fabrication of silicon photonic devices based silicon-on-insulator (SOI) wafers, which is CMOS-compatible and widely used in the laboratory and semiconductor industry, to fabricate integrated silicon nitride device, in particular high Q-factor ring resonators realizing four wave mixing, is still challenging.

Collaborating with Yokoyama Lab in Kyushu University, we perform the subtractive fabrication of silicon nitride ring resonators as well as other optical devices. To discover the diversity of fabrication recipes and compare the material properties, we also design the device layout and order the devices using ligentec process and NTT-AT process.

4.1 Subtractive fabrication process

The subtractive process refers to the subtraction of unnecessary parts after the patterning, differing from the lift-off or damascence processes. For optical waevguides, it challenges the etching process to achieve less roughness on the sidewalls. The previous work using similar fabrication processes reported silicon nitride ring resonators with Q-factor up to 5.2×10^4. The measured loss of waveguides is 2.9 dB/cm [22].

The schematic process flow of the subtractive process is shown in Figure 4.1. First, the silicon dioxide film is deposited on a 4-inch silicon substrate using the TEOS (tetraethyl orthosilicate) source. An alternative method is using a thermal oxidized silicon wafer directly. The target thickness of silicon dioxide layter is greater than 2 µmto create enough buffer between the silicon nitride film and the silicon substrate. Next is silicon nitride film deposition using chemical vapor deposition methods. Following electron beam (EB) lithography patternning, the silicon nitride layer is etched with inductively coupled plasma reactive-ion etching (ICP RIE) technique. After the resist removal, another layer of silica is cladded. Finally, the chip is cut to couple the light from the edge.

The details of each step will be expanded in the following contents.

4.1.1 Film deposition

Low pressure CVD (LP-CVD) is a traditional method to deposit silicon nitride from the vapor source by the decomposition of chemicals on the surface. Stoichiometric silicon nitride can be obtained by controlling and optimizing the ratio of silicon and nitrogen sources. The precursor of silicon is usually silane (SiH_4) or chloride silane gases, such as dichlorosilane (DCS, SiH_2Cl_2). And the ammonia gas (NH_3) plays the role of nitrogen source.

$$3\,SiH_4(g) + 4\,NH_3(g) \longrightarrow Si_3N_4(s) + 12\,H_2(g)$$
$$3\,SiH_2Cl_2(g) + 4\,NH_3(g) \longrightarrow Si_3N_4(s) + 6\,HCl(g) + 6\,H_2(g)$$

Considering the toxic gases used in LP-CVD, an alternative approach is to use modern plasma-enhanced CVD (PE-CVD) with liquid source, which has faster growing rate and lower reaction temperature.

To compare the CVD method dependence of film properties, especially the refractive index, in our research, three different CVD facilities—LP-CVD, PE-CVD and liquid source CVD (LS-CVD) are exploited with three different recipes to deposit the silicon nitride films.

Compared with commercial silicon nitride on insulator wafers deposited using LP-CVD, the details of PE-CVD and LS-CVD recipes are listed in Table 4.1. It is apparent from the data that LS-CVD has the fastest rate 23 nm/min, and lowest reaction temperature. In addition, during our experiments, although the flow rate of SN-2 source changes the film growing rate, it does not effect the film stoichiometry and optical properties. It is also worth to mention that all the wafer deposited with above three recipes shows no cracks during the fabrication, suggesting low tensile in silicon nitride films.

4.1.2 Material properties

Ellipsometry

It is more necessary to evaluated the refractive indexes of the film deposited above. Using the infrared elliposometry, the refractive index of deposited silicon nitride film is obtained. The result is shown in Figure 4.3, where we can see the index varies from the deposition methods at the magnitude of 0.01. Furthermore, even the refractive index are distinguished, the material wavelength dispersion parameter D_M can be close.

Fourier-transform infrared spectroscopy

The vast majority of studies on silicon nitride fabrication processes have found that the hydrogen remaining in the films leads to N-H and Si-H bonds, which causes the optical absorption at S and C band [23, 24]. To quantitatively clarify these bonds in our film, we perform the Fourier-transform infrared spectroscopy (FTIR) on the top of silicon nitride film.

The measurement is carried out using attenuated total reflection (ATR) method with SHIMADZU IRTracer-100. In Figure 4.2, the absorbance is taken from the difference with background transmittance. It can be seen that except the peak around 780? cm^{-1} referring to Si-N stretching mode, two other peaks are located around 2150 and 3350 cm^{-1}, corresponding to Si-H and N-H bonds respectively.

Interestingly, there are also two peaks found at 1020 and 1120, indicating Si-O symmetric and asymmetric stretching modes. This result may be explained by the fact that in ATR method, the depth of penetration at this wavelength is less than 1 micron, while the thickness of silicon nitride layers in our experiment is targeted at 800 nm.

In conclusion, even though the ammonia free recipe is used in LS-CVD method, the film is still hydrogenated while LP-CVD commercial wafers show least N-H absorbance.

4.1.3 Patterning

The sample used in our experiments are usually in the size of 20 mm × 20 mm, diced off from a 4-inch wafer. Before the electron beam lithography, electron beam resist is spin-coated on the surface of silicon nitride films after several times of cleaning.

But first, a layer of an adhesion promoter, hexamethyldisilazane (HDMS) is coated at 2000 rpm and then baked at 120 °C for 1 min. Next, the positive resist (AR-P 6500, ALLRESIST GmbH) is coated at 1000 rpm and soft-baked at 120 °C for 2 min. The final thickness of resist is around 800 nm to achieve enough thickness during the etching process. The main EB machine used in our experiments is ELIONIX ELS-F100 and the beam dose is 3 nA, 0.6 sec/dot. This recipe is fully optimized and has small feature sizes and high accuracy around 10 nm. After the lithography, the sample is developed using *o*-xylene.

4.1.4 ICP etching

In order to etch the waveguide layer selectively, ICP-RIE (RIE-400iPB, SAMCO Inc.) is used to remove the unmasked section in silicon nitride layer.

Different from previous work [6], the ICP-RIE facility used in this study is optimized for deep silicon etching. In the key etching step of our recipe, only CHF_3 gas, 6 sccm, is used along with argon gas to cleans any residual organic matter over the surface. ICP power is set 50 W, and RF bias power is 20 W.

The etching rate of three kinds of film is listed in Table 4.1. From the data, we can see LS-CVD deposited film has the best selectivity, much higher than LP- and PE-CVD samples. It seems possible that the film density varies from the CVD methods, due to LS-CVD has the fastest growth rate and lowest reaction temperature.

4.1.5 Top-cladding and annealing

The final step is cladding another layer of silicon dioxide. To remove not only the residual EB resists but also the polymer generated during the plasma etching, all the samples are first deeply ashed using normal oxygen recipe in another RIE facility. To reduce the damage to the waveguide shape during ashing, organic cleaning is supplied. As same as the buried oxide layer, TEOS source is used to deposit a 2-3 μmtop cladding layer with the same LS-CVD facility.

To remove the residual hydrogen in silicon nitride film, an optional step of annealing is necessary.

Traditionally, annealing process can be performed in different cases, after or during CVD deposition [25], after dry etching or after top cladding [26]. Since the first case requires tensile control during cycled deposition-annealing operation [25], in our experiments, annealing before or after top cladding of negatively patterned LS-CVD and PE-CVD sample are merely compared.

To achieve high vacuum during the annealing, we use a tube-type electric furnace. In a high vacuum, the furnace is set first heating gradually from room temperature to 300 °C for 1 h, then heating to 1000 °C for 3 h, keeping at 1000 °C for 4 h, and cooling down to 300 °C for 5 h, then naturally cooling to room temperature.

Shown in Figure 4.4, there are cracks on both the LS-CVD and PE-CVD samples. In contrast, the negatively patternned samples are free of any cracks but is severely contaminated, which possibly results from the contamination in the tube furnace. In general, the finding of cracks on the top clad layer shows despite the tensile control over the silicon nitride film, even negative EB resist is used for transferring the structure, it is still difficult to annealing the typical TEOS cladded samples with the PE-CVD facility in our fabrication condition.

4.1.6 Edge coupling and chip dicing

To achieve high coupling efficiency, we adopt monolithic inversed tapered waveguide as the mode convertor. The input and output ports of waveguide are both tapered from normal width 1.5 µmto a narrower end. By FDTD methods, the mode field is swept with different taper end widths.

From the result shown in Figure 4.5a, the mode fields expand horizontally as the taper end width increases proportionally. The largest mode size of 3.4 µm× 3.4 µmis successfully demonstrated, but the enhancement is not significant compared with no tapered port in Figure 4.5e. In result, a lensed fiber with spot diameter from 3.0 µmto 3.4 µmis recommended.

In order to precisely define the input and output ports, the chip dicing is required. Compared with conventional mechanical dicing, the laser dicing technique is advantageous at high precision and less damages on the chip edges. The image of laser diced edge is compared with the manually diced one in Figure 4.6. Apparently, the chip using laser dicing has smoother edge, which is helpful to reduce the backward scattering.

4.2 Fabless samples via foundries

Fabless photonic research is becoming a trend for its cheaper and easier external run [27]. There are several foundries all around the world offering the multi-project run service on integrated photonics and quantum optics applications, such as AMF in Singapore, Ligentec in Switterland, LioniX in Netherlands and etc.

Based on the silicon nitride platform, two independent foundries are evaluated in the following sections in the term of device performance and fabrication techniques.

4.2.1 Ligentec technique

Photonic damascene process [28, 29] used in Ligentec samples improves the waveguide sidewall roughness by depositing the silicon nitride film into the etched thermal oxidized silica. By additive chemical mechanical planarization (CMP), the top surface of silicon nitride is improved.

The sample layout is illustrated in Figure 4.7. Five groups of various FSRs are designed. In ecch specific group, the coupling gap is detuned gradually from 400 nm to 700 nm in the step of 100 nm.

The microscope images of the samples is shown in Figure 4.8. Several layers of different structures are observed hierarchically, including the cross pattern stopping the crack during annealing and CMP, the silicon waveguides and a top unknown metallic layer.

4.2.2 NTT-AT technique

NTT-AT technique adopts a different physical vapor method–reactive sputtering to deposit non-hydrogen silicon nitride. Compared with standard silicon sputtering, the nitrogen flow is supplied and reacts with silicon vapor into the silicon nitride film. The refractive index of the film deposited using method is also shown in Figure 4.3.

In the term design, the 4-inch wafer is customed with 22 cell in the layout shown in Figure 4.9, including the same design of Ligentec one in the special cell.

Chapter 5

Device evaluation and dispersion analysis

In the example given in Section 3.2, a typical dispersive ring resonator has the D_2 value less than MHz, which means the frequency FSR, for example 100 GHz, is different from the next one with a MHz-level difference. It is difficult to achieve such precise measurement using traditional optical spectrum analyzer whose typical resolution is around pm, 100 MHz. The tunable laser scanning is developed to solve this problem, especially assisted by an external frequency comb [30].

Here, we exploit the method using laser step triggering to calibrate the real-time measured device transmission. Compared with the frequency comb or wave meter assisted spectroscopy, this method is much more convenient to deploy. By increasing the data acquisition sampling rate or altering with electric oscilloscope, the wavelength precision can be further improved. Given the well-resonant spectrum, the dispersion information is further extracted from the transmission, in particular the resonant peaks. Such method is widely used to study the Kerr frequency comb. It is also efficient to study the frequency-entangled photon pair generation.

5.1 Methods

5.1.1 Fiber launching

Much of related works, concerning such as photonic crystals or whispering gallery mode resonators, use prism coupling or tapered fiber coupling for coupling tunability. In the case of integrated ring resonators, the bus wavegudies are designed in the distance of several gaps, usually varying from under-coupling to over-coupling. Thus, the light confined in the bus waveguide can be directly coupled inwards or outwards using appropriate optical fibers. In previous works [31], both grating coupling and edge coupling were adopted. However, considering the broadband frequency conversion motivation, the edge coupling is preferred for a comparatively broader 3-dB bandwidth.

Using two five-axis fiber alignment stages (Newport M-562F-XYZ & M-562F-XYZ-LH), the device ports are aligned with two lensed fibers on both sides. The spot size of lensed fibers is 2 μm, which is not optimized to the size mentioned in subsection 4.1.6.

Before any following experiments, the output port is first coupled to the infrared InGaAs camera in free space using a 20× objective lens. To align the chip input port precisely, the real-time camera images is used to adjust all the three degrees of freedom until the spot is observed explicitly on the screen. Next, by carefully rotating the palettes of polarization controller on the input side, the device coupling can be launched in either TE or TM mode. Then another lensed fiber is launched instead and aligned carefully, as the power meter reading is referred to.

In this method, the best facet-to-facet coupling efficiency is around 6 dB in the case of ligentec samples, where is optimized by mode convertors. Comparatively, a more typical facet-to-facet loss without mode convertors can be 8-9 dB.

It is worth mentioning that the chip arrier (SURUGA SEIKI F126) is equipped with a thermoelectric cooler (TEC), which is essential for long-time thermal stability. With connected to an external temperature controller, the temperature precision over device under test can be 0.1 °C. To avoid moisture condensation, the TEC is set a little higher than room temperature, 30 °C in our case.

5.1.2 Spectrum sweeping

The schematic diagram of the device spectrum measurement is shown in Figure 5.1. After manual alignment, the TSL (SANTEC TSL-710) is first set to continuously sweep from 1480 nm - 1640 nm, covering the telecom S C and L bands. The internal power reference signal and the step trigger are also generated simultaneously, which are used to calibrate the output optical power and improve wavelength scanning accuracy. The output power from device under test is measured by the power meter (Newport 2963-R).

Compared with photon diodes, the power meter in our setup is critical to realize various range scanning. Finally, the signals from power monitor, step trigger and device transmission are all synchronized with the data acquisition module, and then analyzed by the computer. To achieve pm-resolution spectra, transmitted power is simply divided by power reference and the step trigger are marked to interpolate wavelengths in the certain time interval.

5.2 Thermal stability

Although silicon nitride is reported as high thermal conductivity material, the surrounding silicon dioxide is comparatively worse thermal conductive. Despite the room temperature fluctuation, the nonlinear phenomena usually requires high pump power intracavity, which heats the device significantly, the index change variation leads to resonance shift. Thus, the thermal sensitivity is a critical factor of nonlinear ring resonators.

For example, with the TEC set into different temperatures, the spectrum of a LP-CVD sample is then measured. Shown in Figure 5.2a, temperature increasing leads to a obvious red-shift of the resonant peak. The wavelength range around 1630 nm is chosen for better transmission and well resonance in this device. From Figure 5.2b, the estimated thermal dependence of resonant wavelength $\mathrm{d}\lambda/\mathrm{d}T$ is 23 nm/°C. In this case, if the Q-factor of ring resonator is up to 10×10^5, even room temperature variation can results in resonance totally mismatching at pumping wavelength.

5.3 Device transmission

Given the transmission spectra, the negative peaks are located with peak-finding algorithm, yielding not only the peak location, but also the width and prominence. These values are next used to calculate the free spectral ranges and Q-factors. In general, due to the fabrication difference, not all the device appear resonance all around the measured band. To compensate the broken spectra, several algorithm are performed to achieve best performance of peak-finding.

In our technology, for the spectra with remarkable absorption illustrated in Figure 5.3, the background of raw spectrum is first calculated using digital filters. The filtered spectra to search the peaks are then the difference between raw spectrum and background without the noise effects.

5.3.1 Subtractive fabricated samples

To compare the material difference among the films deposited in three CVD methods, identical ring resonators layout is used to fabricate all these samples. Since the thickness control during the film deposition and ICP etching is tough, all the device are label with the waveguide height measured by step profiler before TEOS top cladding. However, the fabrication of stoichiometric silicon nitride using PE-CVD method is not successful, a sample deposited using same machine but with a silicon-rich recipe is reported instead.

The device transmission spectrum is first measured, shown in Figure 5.4(a). It can be seen that there is strong optical absorption from 1520 nm to 1540 nm in each device. Compared with the FTIR result shown in Figure 4.2, in particular the case of LP-CVD sample where is almost no Si-H or N-H bonds found, the absorption not only originates from the residual hydrogen but also may suffer from top-cladding or bottom buried TEOS layer.

In addition, LP-CVD sample shows absorption at some certain wavelength, leading to the error values of peak finding. Such kind of broken spectra can be probably explained by the fabrication toleration, such like the gap is not fully etched or the ring resonator is contaminated with a certain particles. All these fabrication imperfection plays the role of scattering and also decreases the quality factors.

Furthermore, from the extracted resonant peaks, the Q-factors and frequency FSRs are summarized in Figure 5.4(b). The radius of each ring resonator are designed as 200 μm, corresponding to the FSR of 119.3 GHz. This agrees with the extracted FSRs of LP-CVD and LS-CVD samples. In the case of silicon-rich PE-CVD sample, the measured FSR of ring resonators near 1550 nm is around 94.3 GHz, indicating the refracting index of silicon-rich silicon nitride film is 0.34 higher.

In the term of Q-factors, counted in Figure 5.4(c), the LS-CVD samples have the highest quality values at the mean of 3×10^4 while the one of silicon-rich PE-CVD samples is near to 1×10^4. The distribution of LP-CVD sample are similar to LS-CVD ones, but influenced by the broken resonance spectrum. The tendency of Q-factors is as same as the transmission.

5.3.2 Fabless samples

Coupling evolution

Prior to cavity properties evaluation, it is essential to compare the coupling condition among devices in the same group. Since the gap between bus waveguide and ring resonator is swept increasingly, usually the coupling condition turns from over coupling to critical coupling, and finally into weak coupling.

For the Ligentec group 1, due to the reliable fabrication recipe, such an evolution of coupling condition among the same group is explicit as the gap increases. As presented in Figure 5.5(a), the coupling condition varies from over coupling to critical coupling, as the negative prominence of resonance peak increases. The same tendency agrees with the Q-factors, shown in Figure 5.5(b). The other groups in the sample have the similar tendency but the critical coupling gaps are different.

Quality factor comparison

Several works using the same Ligentec technique report ultrahigh Q-factors up to 3×10^6 [32, 33]. The same magnitude is also attained in our samples in Group3 and Group5. While to compare the fabrication quality of both technique, two device with the same design (Group1 Device4, gap 700nm, FSR 100 GHz, ring width 0.8 μm) are listed in Figure 5.6, as well as the Q-factor histograms.

In the transmission of Ligentec device, shown in Figure 5.6(a) and NTT-AT device shown in Figure 5.6(b), there is no obvious absorption in the range 1520 nm - 1540 nm compared with the samples fabricated using non-annealing subtractive recipe, though the transmission background declines at both red and blue side. However, the quality factors of Ligentec one are almost 4 times of NTT-AT samples, indicating the intracavity loss is 4 times lower. The histogram gathered in Figure 5.6(c) and Figure 5.6(b) features the same result. In both samples, the critical coupling features at shorter wavelength, according to the peak prominence and Q-factor tendency.

We assume that despite the ammonia-free recipe used in NTT-AT technique, the etching recipe is not as fully optimized as Ligentec ones. It is also interesting to find that there is a clear difference of FSR trends from the former. In particular, the increasing NTT-AT FSRs indicate a normal dispersion.

5.4 Dispersion analysis

Previous work [31] gave two methods analyzing the device dispersion, both depending on device transmission. One is to perform Fourier transform of the reflected spectra on the input port, which is equivalent to an etalon interference whose mirrors are waveguide input and output facets. Another method is similar but employs the cavity resonance instead. Despite the fabrication tolerance, considering the bent segment, the chromatic dispersion in the ring resonator is not identical to the one in straight waveguides. Hence in our research, to the extract dispersion information accurately, the ring resonance method is preferred.

Following the integrated dispersion definition, the resonant wavelength λ_m is first converted to resonant frequencies ω_m. Before the polynomial fitting, the linear fitting is performed to evaluate first-order mode dispersion parameter. Then the integrated dispersion is calculated using the formula $D_{\text{int}}(\mu) = \omega_0 - D_1\mu$. The central frequency is ω_0 set as the center of scanning range. The relative mode numbers are constructed as a integer neighbourhood of zero. A final step is perform the cubic or quadratic polynomial fitting. For the wide range scanning, a quartic curvature is more efficient, but in our case, the cubic polynomial is sufficient to extract the dispersion parameters at the second order in a 160 nm span.

The identical devices mentioned in transmission comparison section is further analyzed using the above method. The integrated dispersion is extracted in Figure 5.8.

Chapter 6

Broadband photon pair generation

Back to the classical nonlinear optics theory, the solution to nonlinear coupling equations requires the initial power at ether signal or idler mode, which is called seed in the laser terminology. However, in quantum classical theory, all the modes in cavity behave intrinsic vacuum fluctuation at the quantity of half $\hbar\omega$. Thus, even without light fed, the quantum fluctuation leads to enhancement at the single photon levels. The intracavity pump power then behaves the amplifier, intensify the corresponding signal or idler mode photon flux. Once the single photon flux exceeds cavity threshold, the extracavity single photon can be detected. To note, these kind of excitation is indistinguishable because the signal and idler photons are emitted simultaneously as a result of quantum mechanics, rather than signal photon stimulates idler photon and vice versa. In the context of quantum states, the state created intracavity is at the superposition of signal state and idler state. The wave packet is different from the normal single photon one. Further theoretical research [34] explained the squeezed nature of four wave mixing photon pairs, which is one of the exclusive properties of frequency entangled photon pairs.

In general, the spontaneous four wave mixing in nonlinear cavities defined in our context refers to the cavity modes are excited collectively and pair-by-pair under the phase matching condition. Thus, under the weak coherent approximation, the photon pair only include one photon in each mode but correlated with each other. Thus, the conventional coincidence counting technology can be used to verify such correlation. In the term of generation band, it agrees with the classical phase matching condition at pump power limit.

6.1 Methods

Using the dispersion extraction method in previous chapter, zero dispersion wavelength can be located easily among the measured band. Optical telecom band is focused on in this research due to enormous available fiber optical components for totally in-line setups. Illustrated in Figure 7.1, the setup of mode-resolvable singular photon pair generation adopts the tunable laser as the pump source whose display tunability is 0.1 pm. The laser output is first connected to ring resonators using the same fiber launching system and measured with the power meter. A simple transmission scanning is perform to select the built-in polarization. For the high Q-factor devices, the transmission of TE and TM modes are separated in a distance of tens of pm. Thus, as either of the resonance vanished, the input polarization is aligned at particular mode. For low Q-factor cavities, the method of polarization alignment is as same as the one used in spectra transmission scanning.

Next, the output light are splitted 50%:50%, indicating half of photons are lost, and sequentially filtered through two sets of band pass filters. The 3dB bandwidths of first set are 1540±4 nm and 1560 ±4 nm, respectively. The second ones are tunable and 0.12nm-wide. Since the mode spacing is 0.75 nm for 100GHz-FSR cavities, the tunable band pass filter is adequate to define the single mode. Finally, each channel are detected using superconducting single photon detectors (SNSPD) in the resolution of 100 ps. Since the SNSPD is polarization-sensitive, another two polarization controllers (not shown) are used to achieve highest single photon counting. The time controller (ID900, ID Quantique) collects and records the count signal to calculate the coincidence counts.

Coincidence counting

In quantum optics, coincidence counting is usually used to examine the non-locality of singular wave-particle. In our case, the photons splitted into two channels A and B, yields the count per second N_A and N_B. Define the coincidence windows t 1 ns commonly, and coincidence count (CC) is two photon trigger events within this time window, equivalent to the photon pair generation rate effectively. The accidental counting (ACC) is defined as $N_A N_B t$. To reduce the noise effect, accidental-coincidence ratio (CAR) is defined as (CC-ACC)/ACC.

It is worth to mention that in our research, the main topic is generation rather than manipulation, in result numerous band-pass filters are exploited to realize mode-resolvable single photon counting. It does not contradict with distinguishability nature of frequency correlated photon pairs.

6.2 Single mode photon flux

With the pump power set as 100 µW and central wavelength at 1550.64 nm, the result of photon flux versus relative mode index is presented in Figure 7.2. The device selected has FSR of 150 GHz and shows anomalous dispersion around 1550 nm. According to the 3dB-bandwidth of BPFs, the accessible relative mode index corresponds 7-14. To achieve higher photon counting, the central wavelength of TBPFs is tuned carefully in the step of 0.01 nm.

In the result, there is trend that both signal and idler photon fluxes decreases as the mode index increases. It can be explained that phase mismatch of farther modes is greater than closer ones. The difference between signal and idler bands origins from the asymmetry of phase matching condition and filter spectral shape.

6.3 Coincidence counts of singular mode pair

In coincidence counts are measured in a 1 ns coincidence windows and in each mode, the time delay is set from -200 to 200 ps. The Figure 6.3 shows the result of CAR. As the mode number increases, coincidence counts varies roughly but in the CAR graph, such a trend is not obvious. The inconsistency may be due to the instability of pump mode resonance.

6.4 Pump power dependence

Chapter 7

Towards intermodal and intramodal photon pair

7.1 Spontaneous four wave mixing

7.2 Stimulated four wave mixing

Chapter 8

Summary

Acknowledgements

Nam dui ligula, fringilla a, euismod sodales, sollicitudin vel, wisi. Morbi auctor lorem non justo. Nam lacus libero, pretium at, lobortis vitae, ultricies et, tellus. Donec aliquet, tortor sed accumsan bibendum, erat ligula aliquet magna, vitae ornare odio metus a mi. Morbi ac orci et nisl hendrerit mollis. Suspendisse ut massa. Cras nec ante. Pellentesque a nulla. Cum sociis natoque penatibus et magnis dis parturient montes, nascetur ridiculus mus. Aliquam tincidunt urna. Nulla ullamcorper vestibulum turpis. Pellentesque cursus luctus mauris.

Nulla malesuada porttitor diam. Donec felis erat, congue non, volutpat at, tincidunt tristique, libero. Vivamus viverra fermentum felis. Donec nonummy pellentesque ante. Phasellus adipiscing semper elit. Proin fermentum massa ac quam. Sed diam turpis, molestie vitae, placerat a, molestie nec, leo. Maecenas lacinia. Nam ipsum ligula, eleifend at, accumsan nec, suscipit a, ipsum. Morbi blandit ligula feugiat magna. Nunc eleifend consequat lorem. Sed lacinia nulla vitae enim. Pellentesque tincidunt purus vel magna. Integer non enim. Praesent euismod nunc eu purus. Donec bibendum quam in tellus. Nullam cursus pulvinar lectus. Donec et mi. Nam vulputate metus eu enim. Vestibulum pellentesque felis eu massa.

Quisque ullamcorper placerat ipsum. Cras nibh. Morbi vel justo vitae lacus tincidunt ultrices. Lorem ipsum dolor sit amet, consectetuer adipiscing elit. In hac habitasse platea dictumst. Integer tempus convallis augue. Etiam facilisis. Nunc elementum fermentum wisi. Aenean placerat. Ut imperdiet, enim sed gravida sollicitudin, felis odio placerat quam, ac pulvinar elit purus eget enim. Nunc vitae tortor. Proin tempus nibh sit amet nisl. Vivamus quis tortor vitae risus porta vehicula.

References

1. Wengerowsky, S., Joshi, S. K., Steinlechner, F., Hübel, H. & Ursin, R. An entanglement-based wavelength-multiplexed quantum communication network. *Nature* **564.** (2018), 225–228.
2. Tchebotareva, A. *et al.* Entanglement between a Diamond Spin Qubit and a Photonic Time-Bin Qubit at Telecom Wavelength. *Phys. Rev. Lett.* **123.** (2019), 063601.
3. Okano, M. *et al.* 0.54 um Resolution Two-Photon Interference With Dispersion Cancellation for Quantum Optical Coherence Tomography. *Sci. Rep.* **5.** (2015), 1–8.
4. Lu, X., Jiang, W. C., Zhang, J. & Lin, Q. Biphoton Statistics of Quantum Light Generated on a Silicon Chip. *ACS Photonics* **3.** (2016), 1626–1636.
5. Bogaerts, W. *et al.* Silicon microring resonators. *Laser Photonics Rev.* **6.** (2012), 47–73.
6. Ono, Y. *A study of photon-pair generation using silicon nitride ring resonators* Master Thesis (Kyoto University, 2017).
7. Pfeiffer, M. H., Liu, J., Geiselmann, M. & Kippenberg, T. J. Coupling Ideality of Integrated Planar High- Q Microresonators. *Phys. Rev. Appl.* **7.** (2017), 1–8.
8. Leuthold, J., Koos, C. & Freude, W. Nonlinear silicon photonics. *Nat. Photonics* **4.** (2010), 535–544.
9. Agrawal, G. in *Nonlinear Fiber Optics (Fifth Edition)* (ed Agrawal, G.) Fifth Edition, 397–456 (Academic Press, Boston, 2013).
10. Brasch, V. *et al.* Photonic chip-based optical frequency comb using soliton Cherenkov radiation. *Science (80-.).* **351.** (2016), 357–360.
11. Luke, K., Okawachi, Y., Lamont, M. R. E., Gaeta, A. L. & Lipson, M. Broadband mid-infrared frequency comb generation in a Si_3N_4 microresonator. *Opt. Lett.* **40.** (2015), 4823.

12. Xu, Q., Almeida, V. R., Panepucci, R. R. & Lipson, M. Experimental demonstration of guiding and confining light in nanometer-size low-refractive-index material. *Opt. Lett.* **29.** (2004), 1626.

13. Almeida, V. R., Xu, Q., Barrios, C. A. & Lipson, M. Guiding and confining light in void nanostructure. *Opt. Lett.* **29.** (2004), 1209.

14. Mas, S., Caraquitena, J., Galán, J. V., Sanchis, P. & Martí, J. Tailoring the dispersion behavior of silicon nanophotonic slot waveguides. *Opt. Express* **18.** (2010), 20839.

15. Zhang, L., Yue, Y., Beausoleil, R. G. & Willner, A. E. Flattened dispersion in silicon slot waveguides. *Opt. Express* **18.** (2010), 20529.

16. Zhu, M. *et al.* Ultrabroadband flat dispersion tailoring of dual-slot silicon waveguides. *Opt. Express* **20.** (2012), 15899.

17. Nolte, P. W., Bohley, C. & Schilling, J. Tuning of zero group velocity dispersion in infiltrated vertical silicon slot waveguides. *Opt. Express* **21.** (2013), 1741.

18. Zhang, L. *et al.* Generation of two-cycle pulses and octave-spanning frequency combs in a dispersion-flattened micro-resonator. *Opt. Lett.* **38.** (2013), 5122.

19. Herr, T. *et al.* Mode spectrum and temporal soliton formation in optical microresonators. *Phys. Rev. Lett.* **113.** (2014), 1–6.

20. Bao, C. *et al.* Deterministic single soliton generation via mode-interaction in microresonators. **4.** (2018), SW4M.2.

21. Kim, S. *et al.* Dispersion engineering and frequency comb generation in thin silicon nitride concentric microresonators. *Nat. Commun.* **8.** (2017).

22. Cheng, X., Hong, J., Spring, A. M. & Yokoyama, S. Fabrication of a high-Q factor ring resonator using LSCVD deposited Si_3N_4 film. *Opt. Mater. Express* **7.** (2017), 2182.

23. Ay, F. & Aydinli, A. Comparative investigation of hydrogen bonding in silicon based PECVD grown dielectrics for optical waveguides. *Opt. Mater. (Amst).* **26.** (2004), 33–46.

24. Agnihotri, O. P. *et al.* Advances in low temperature processing of silicon nitride based dielectrics and their applications in surface passivation and integrated optical devices. *Semicond. Sci. Technol.* **15.** (2000).

25. Luke, K., Dutt, A., Poitras, C. B. & Lipson, M. Overcoming Si_3N_4 film stress limitations for high quality factor ring resonators. *Opt. Express* **21.** (Sept. 2013), 22829.

26. Wang, L. *et al.* Nonlinear silicon nitride waveguides based on PECVD deposition platform. *Opt. Express* **26.** (2018), 9645.

27. Hochberg, M. & Baehr-Jones, T. Towards fabless silicon photonics. *Nat. Photonics* **4.** (2010), 492–494.

28. Pfeiffer, M. H. P. *et al.* Photonic Damascene process for integrated high-Q microresonator based nonlinear photonics. *Optica* **3.** (2016), 20.

29. Pfeiffer, M. H. P. *et al.* Photonic damascene process for low-loss, high-confinement silicon nitride waveguides. *IEEE J. Sel. Top. Quantum Electron.* **24.** (2018), 1–11.

30. Liu, J. *et al.* Frequency-comb-assisted broadband precision spectroscopy with cascaded diode lasers. *Opt. Lett.* **41.** (2016), 3134.

31. Sunada, Y. *Measurement of Group Velocity Dispersion of Silicon Nitride Ring Resonators toward Photon-pair Generation* Bachelor Thesis (Kyoto University, 2018).

32. Yu, S. P. *et al.* Tuning Kerr-Soliton Frequency Combs to Atomic Resonances. *Phys. Rev. Appl.* **11.** (2019), 1.

33. Vaidya, V. D. *et al.* Broadband quadrature-squeezed vacuum and nonclassical photon number correlations from a nanophotonic device. (2019), 1–10.

34. Scully, M. O. & Zubairy, M. S. *Quantum Optics* (Cambridge University Press, Sept. 1997).

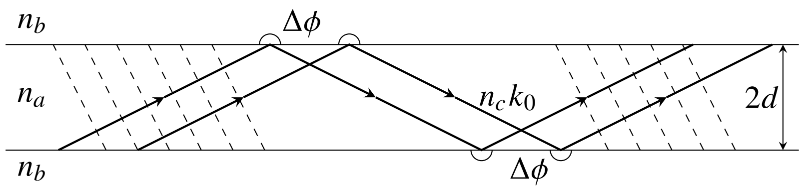

Figure 2.1: **Planar waveguide**. The upper and bottom layer are cladding and the middle is core layer. $\Delta\phi$ represents the Goos-Hänchen shift at the boundary.

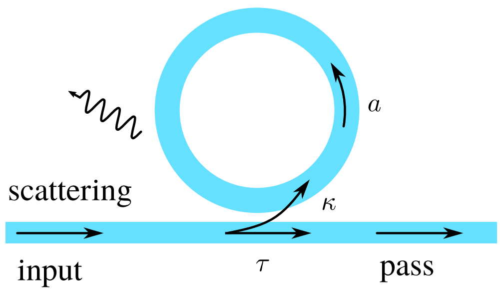

Figure 2.2: **An all-pass type ring resonator**. The transmitted spectrum is filtered periodically by the ring waveguide, in the case satisfying resonance condition.

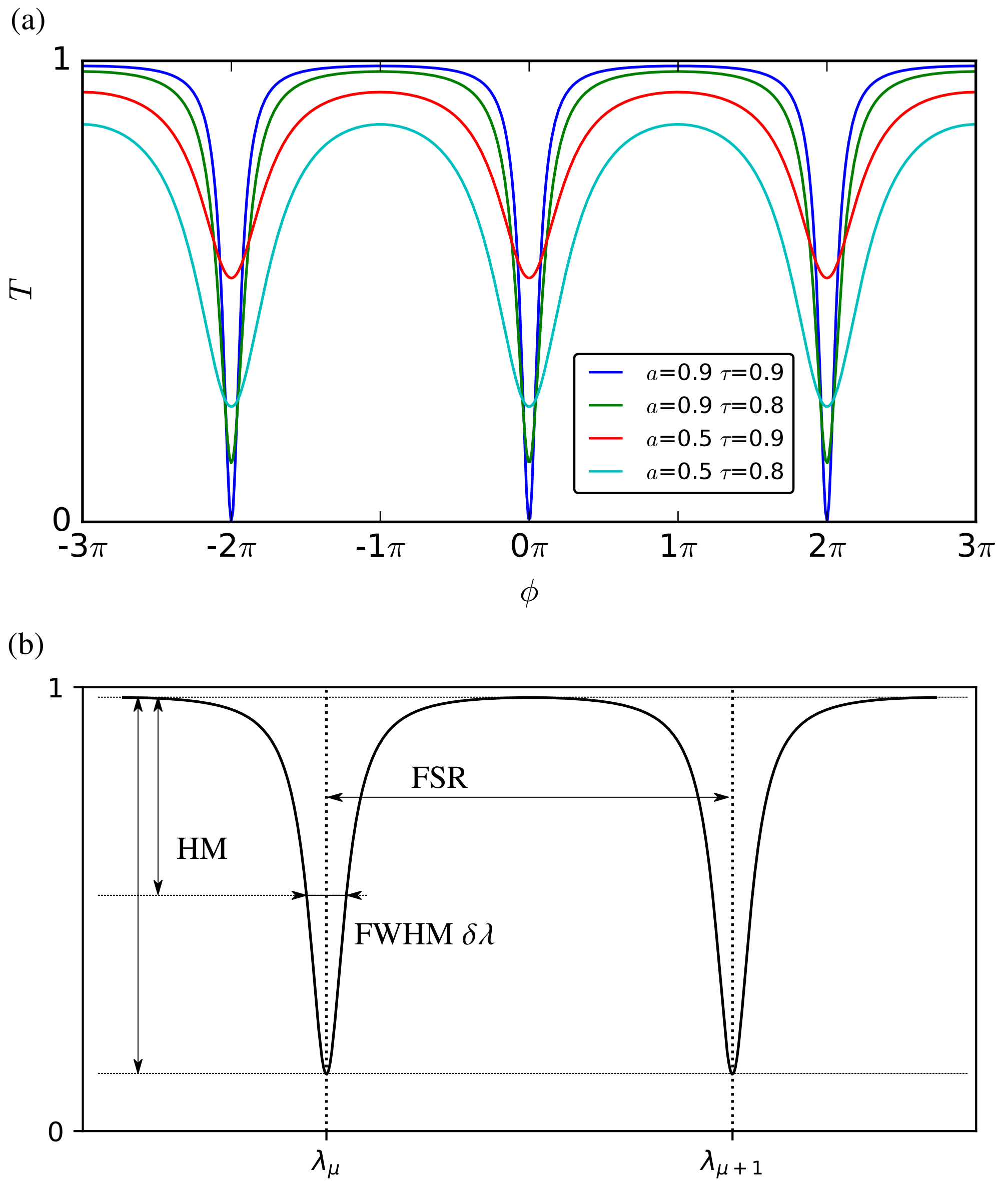

Figure 2.3: **Illustration of wavelength transmission spectrum of ring resonators**. **a**. Coupling condition **b**. FSR, free spectral range, the distance between neighbouring resonant wavelength. FWHM, full width at half maximum.

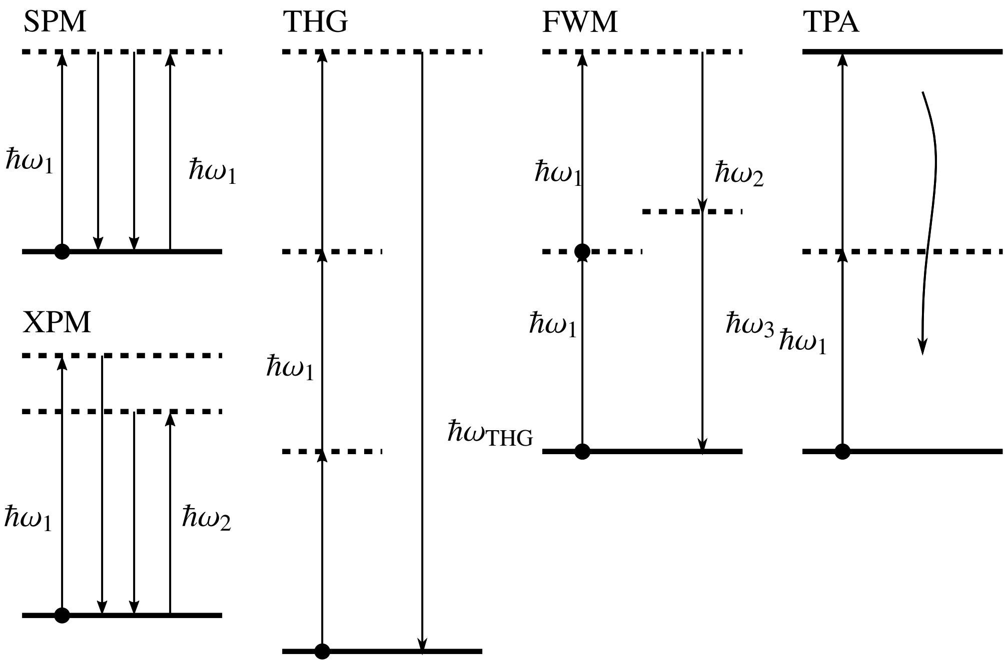

Figure 2.4: **Illustration of possible energy diagram in typical third-order nonlinear processes**.

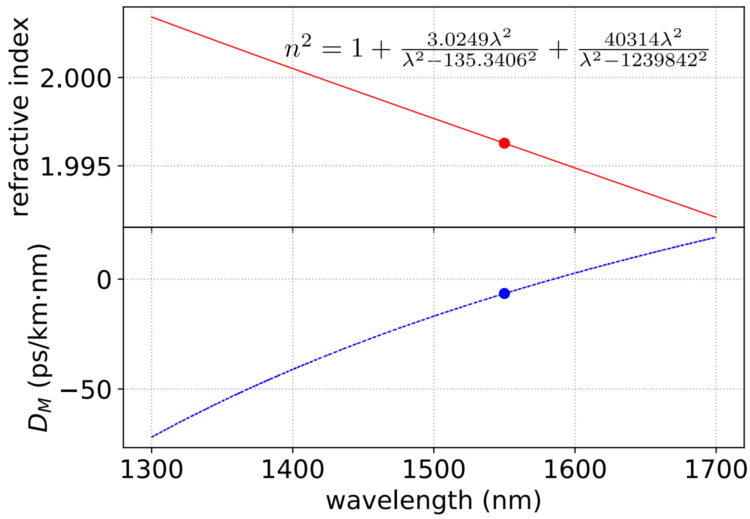

Figure 3.1: **Refractive index and dispersion parameter measured in reference**. λ=1550 nm, n=1.9963 and D_M = -6.5656 ps/(km nm).

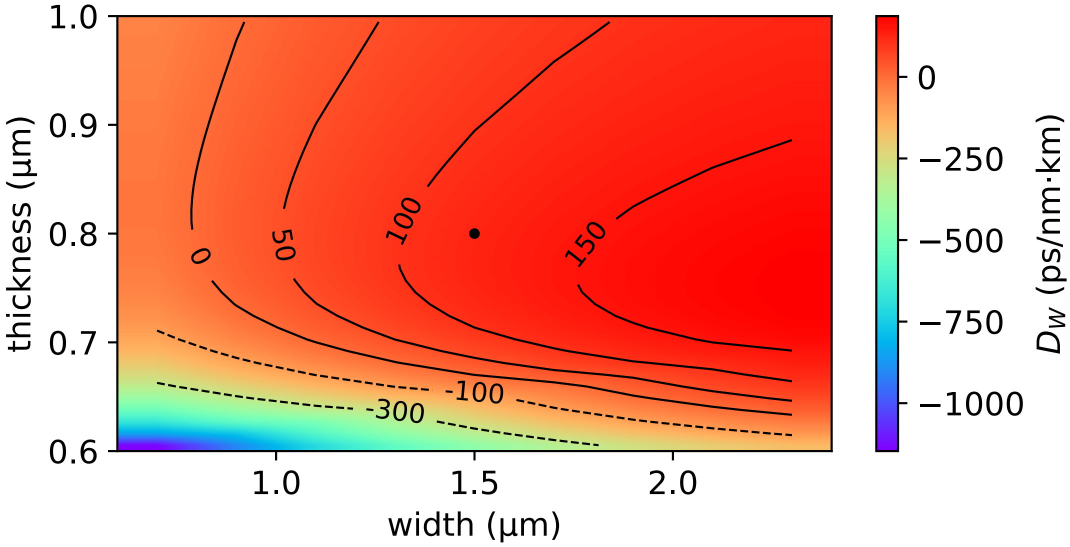

Figure 3.2: **Waveguide dispersion map simulated by Lumerical MODE**. The central wavelength to perform the simulation is 1550 nm and the precision is nm. We select the fundamental TE mode as the objective to study the waveguide dispersion. The scattered point in the figure is 1.5-μm-wide and 0.8-μm-thick.

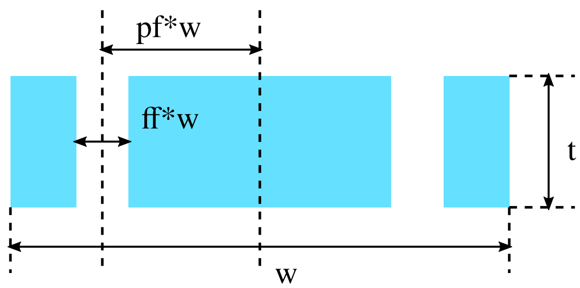

Figure 3.3: **Illustration of a double vertical slot waveguide**. The cyan region is Si_3N_4 waveguide and surrounded by silica.

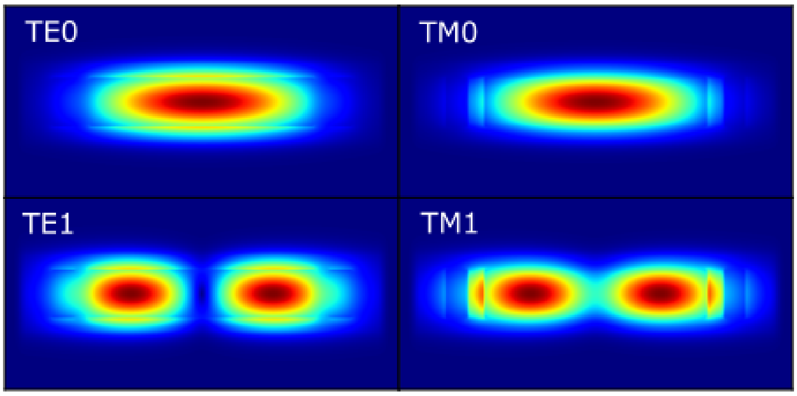

Figure 3.4: **Modes of the double vertical slot waveguide**. w=2.5, t=0.8, ff=0.053, pf=0.4

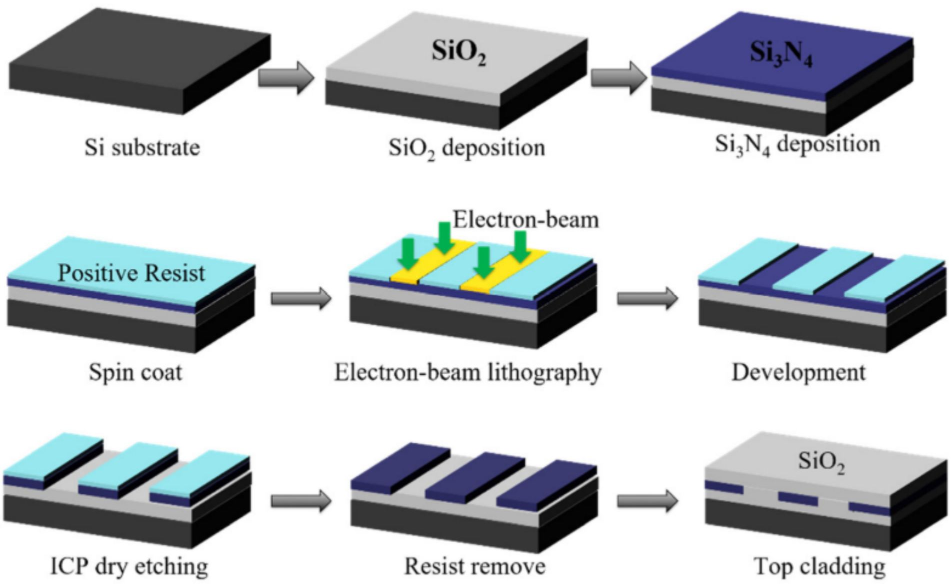

Figure 4.1: **Schematic process flow of the subtractive process**.

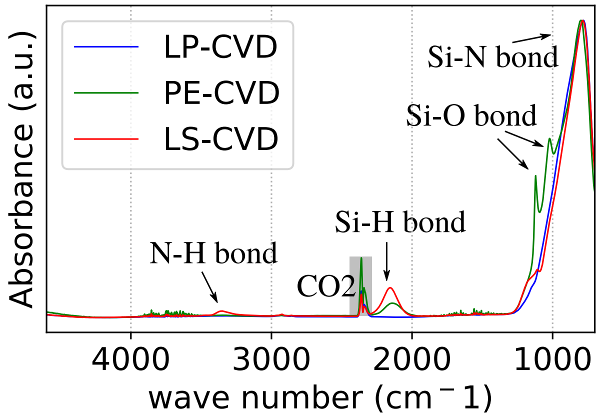

Figure 4.2: Caption

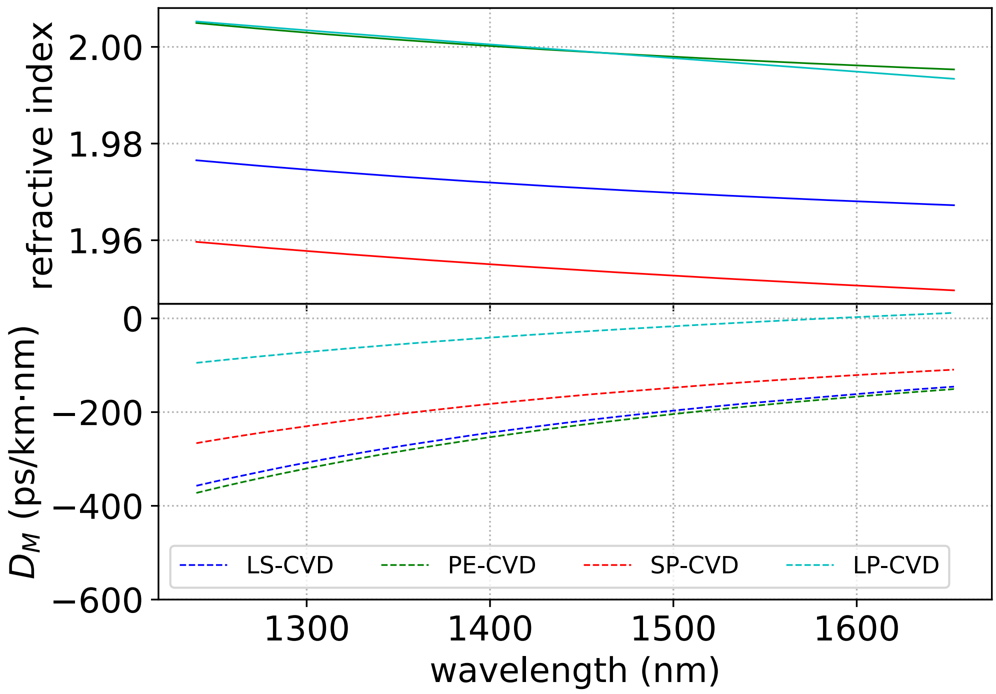

Figure 4.3: **Elliposometry result of the film deposited in several method**.

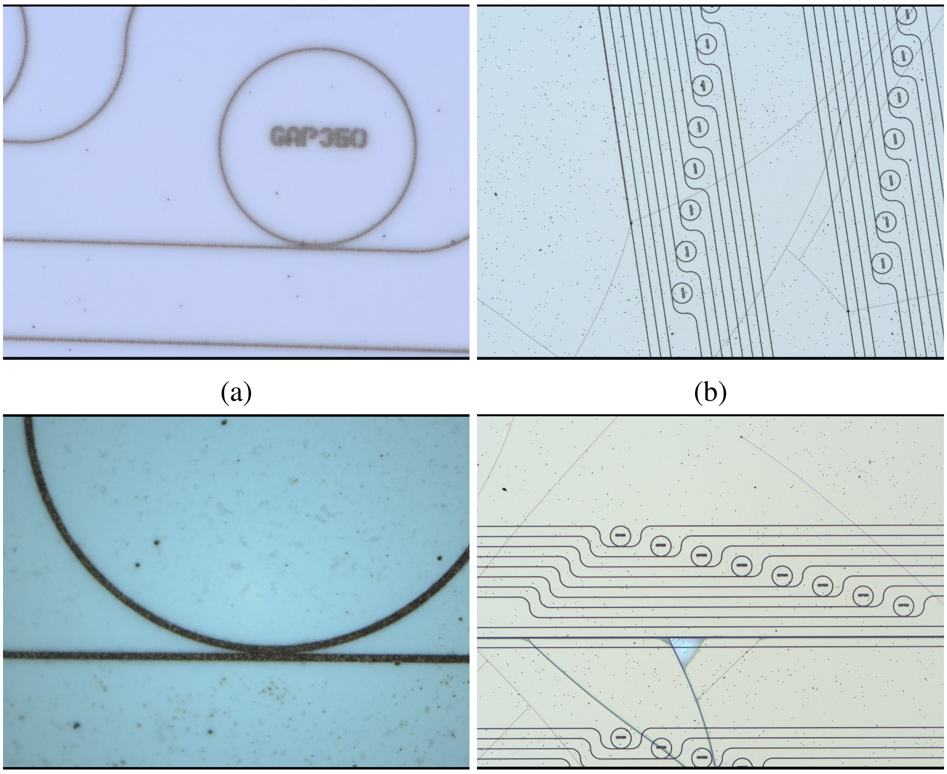

(a) (b) (c) (d)

Figure 4.4: **Laser microscope images of samples after annealing process**. All the sample are annealed under the same circumstance. **a**. LS-CVD sample without top cladding. **b**. LS-CVD sample with TEOS top-cladding. **c**. PE-CVD sampele without top cladding. **d**. PE-CVD sample with TEOS top-cladding.

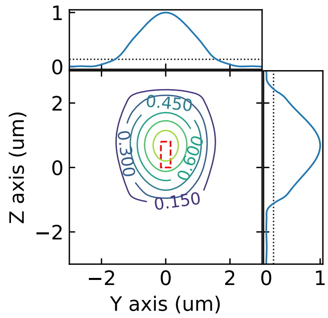

(a) End width 0.3 µm

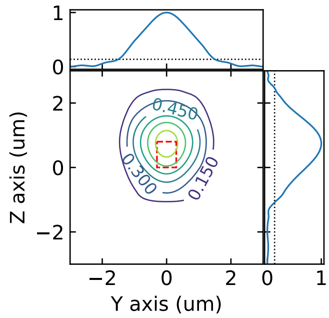

(b) End width 0.6 µm

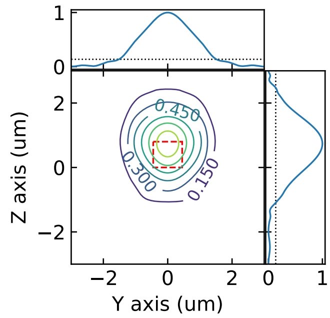

(c) End width 0.9 µm

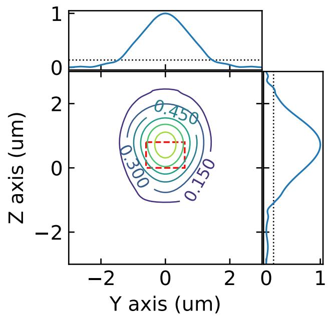

(d) End width 1.2 µm

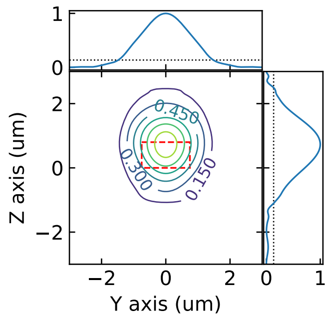

(e) End width 1.5 µm

Figure 4.5: **Mode field at the taper end**. The outline of taper edge is profiled.

(a) Laser diced

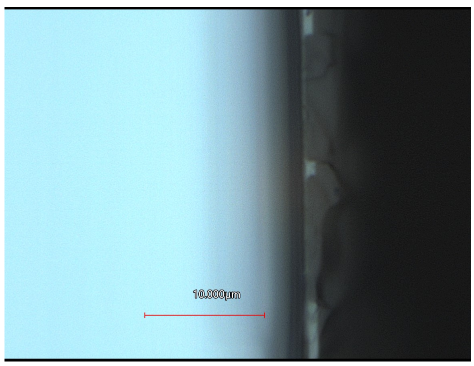

(b) Manually cleaved

Figure 4.6: **Microscope images of chip edge**. The scale in the images is 10 um.

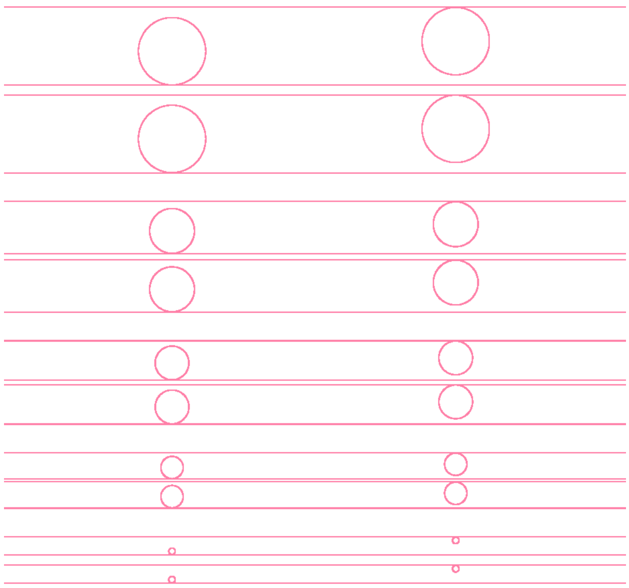

Figure 4.7: Caption

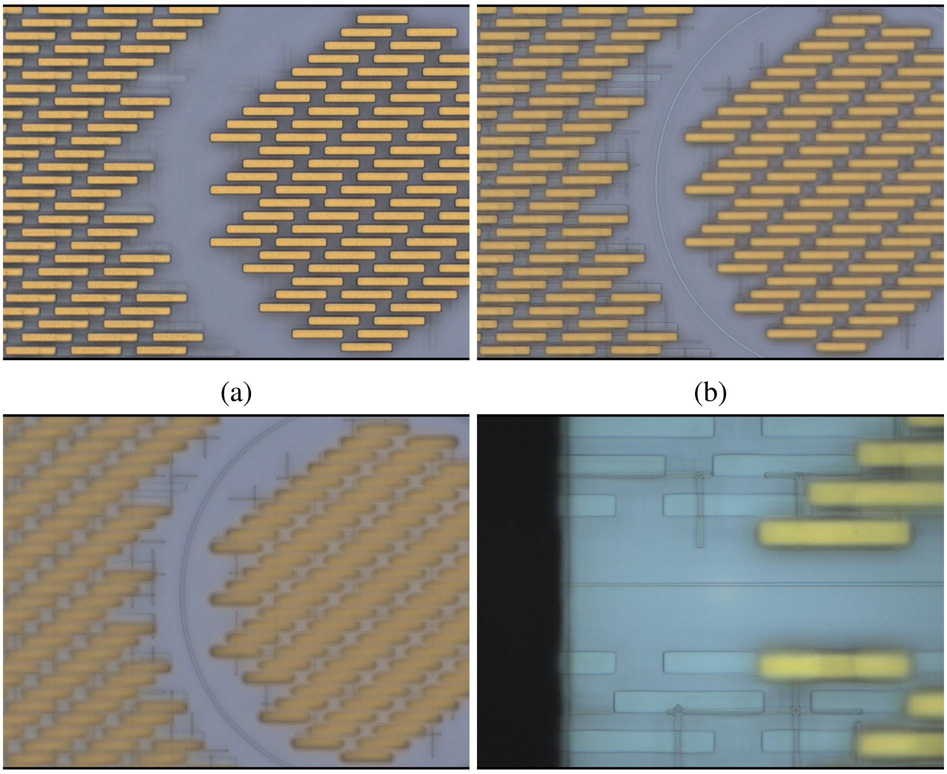

(a) (b)

(c) Crack stopper layer (d)

Figure 4.8: **Laser microscope images of Ligentec smaples**. By lowering the focus depth, three layers are observed. **a**. Top metallic layer. **b**. Device layer. **c**. Crack stopper layer. **d**. Mode convertor

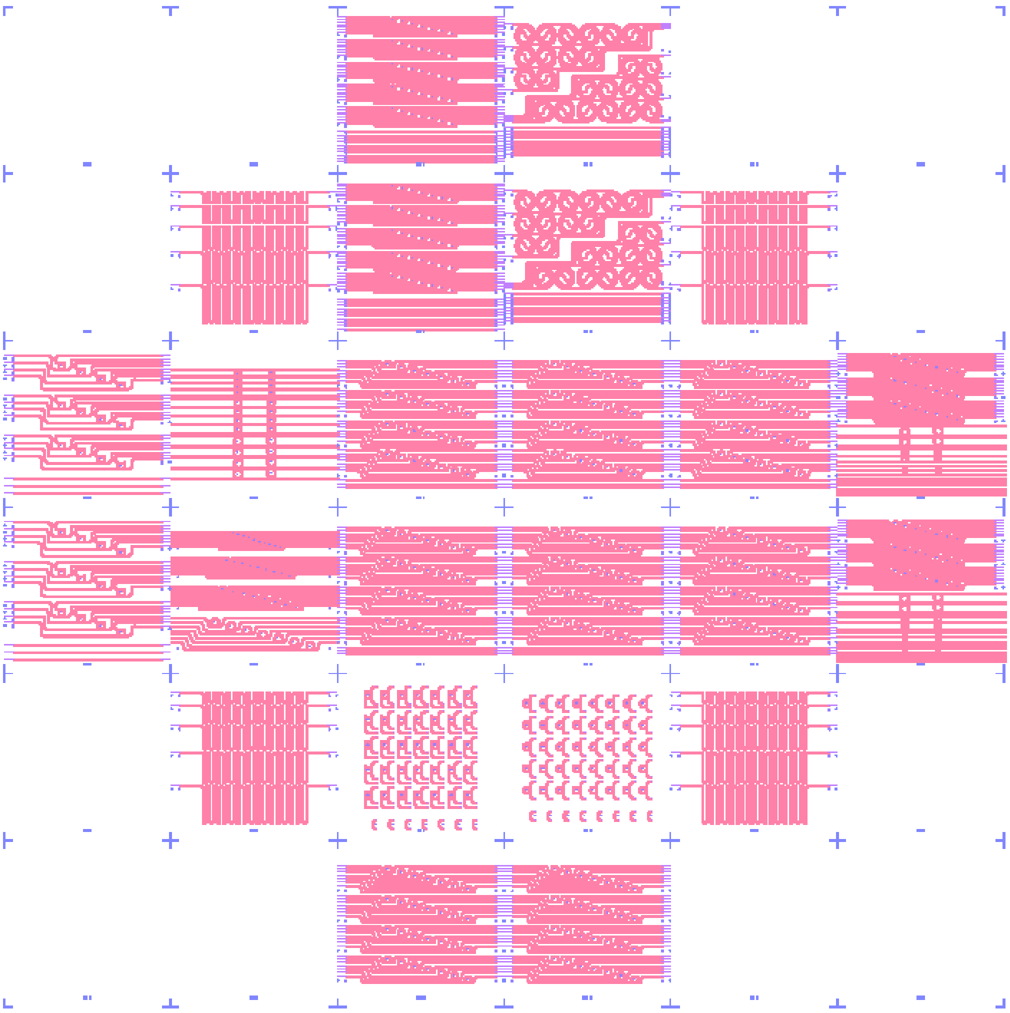

Figure 4.9: Caption

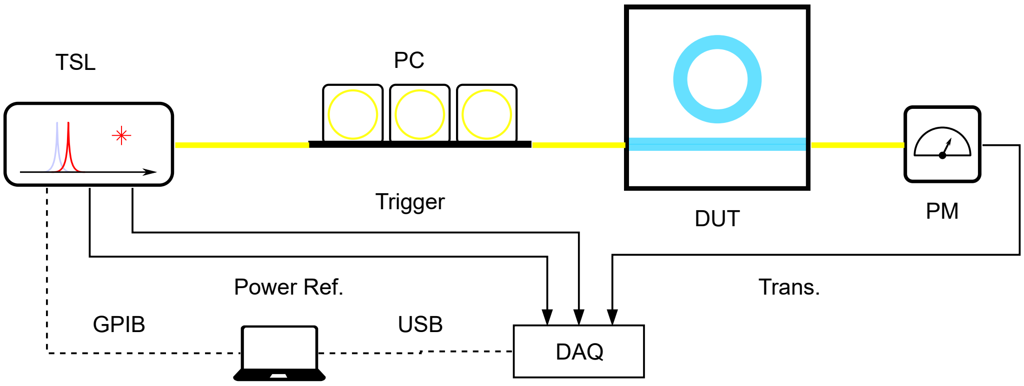

Figure 5.1: **Setup of transmission measurement system**. TSL, tunable semiconductor laser. PC, optical fiber polarization controller. DUT, device under test. PM, power meter. DAQ, data acquisition.

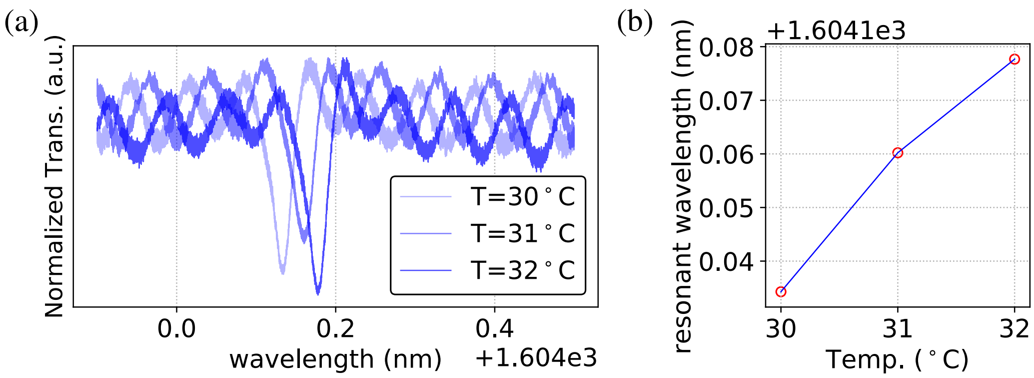

Figure 5.2: **Thermal dependence of LP-CVD sample**. **a**. Transmission measured at three temperatures. **b**. Resonant wavelengths extracted versus temperature. The estimated thermal dependence $\mathrm{d}\lambda/\mathrm{d}T$ is 23 nm/°C.

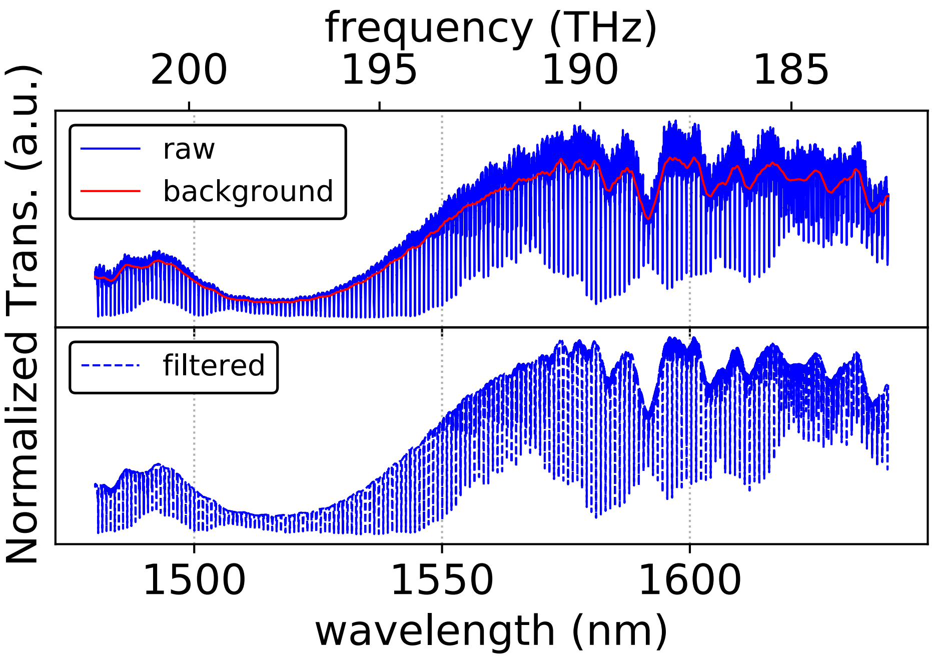
frequency (THz)
200
195
190
185
raw
background
filtered
Normalized Trans. (a.u.)
1500
1550
1600
wavelength (nm)

Figure 5.3: .

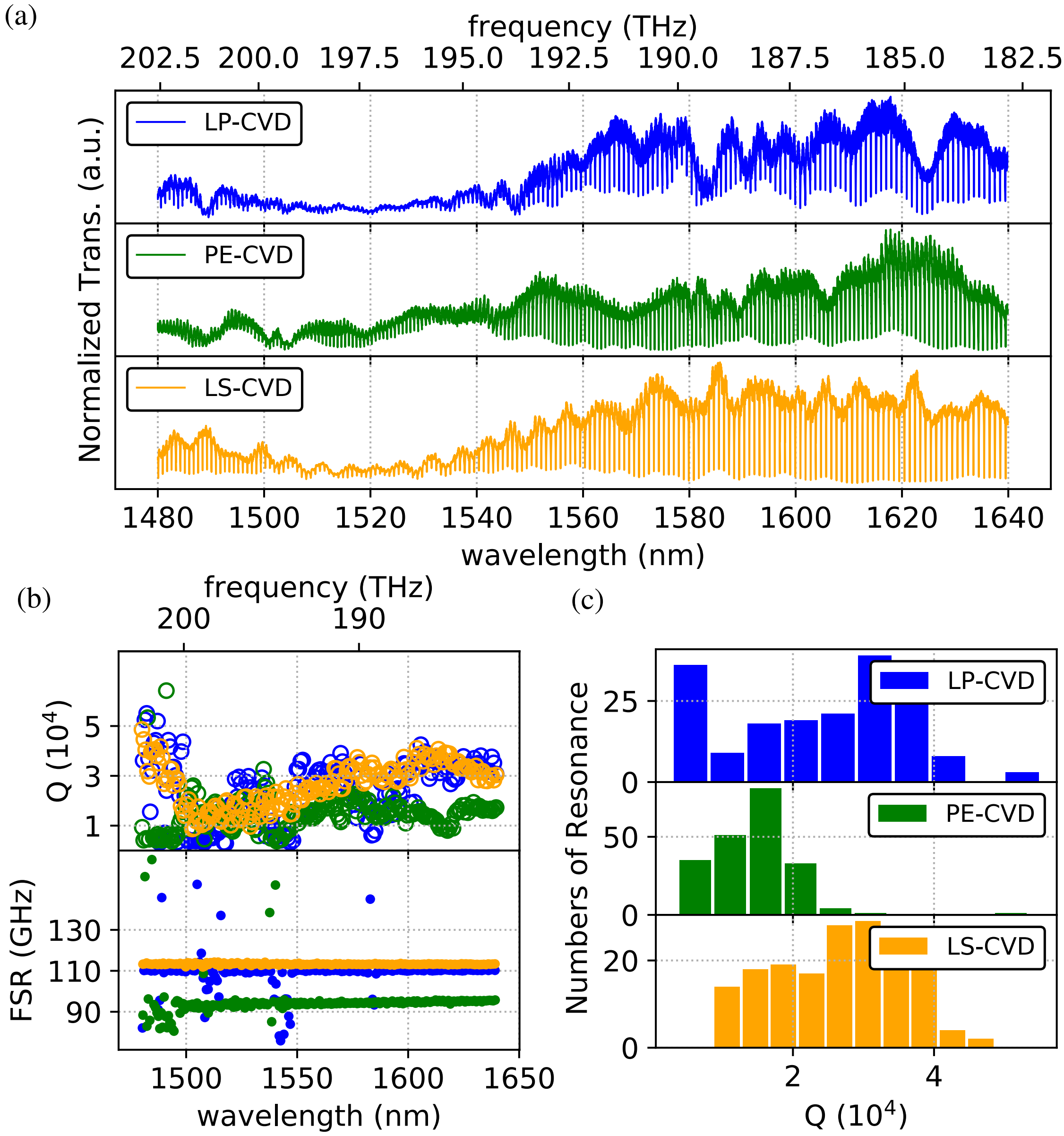

Figure 5.4: **Trans Comparison**.

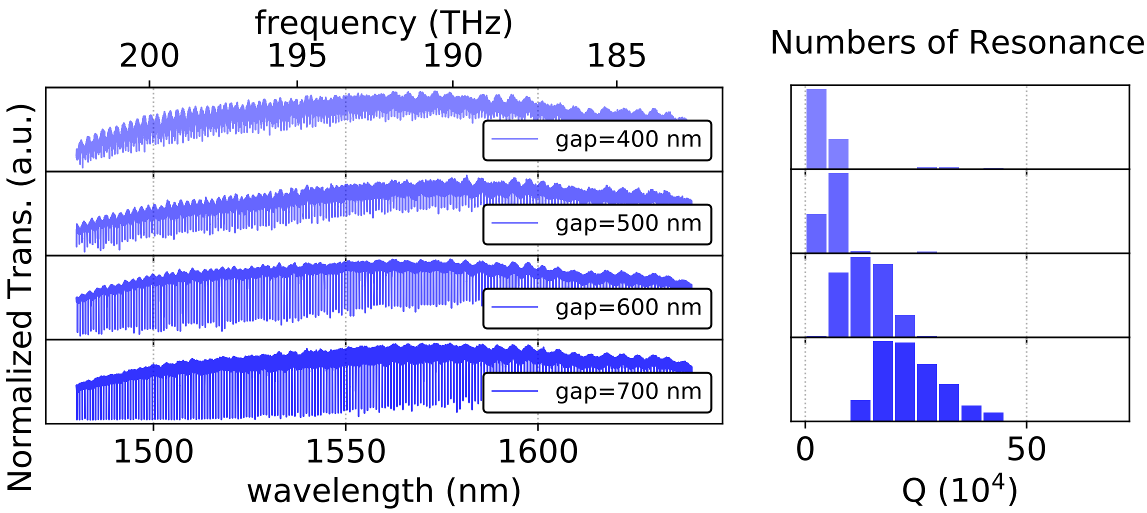

Figure 5.5: **Gap sweeping**.

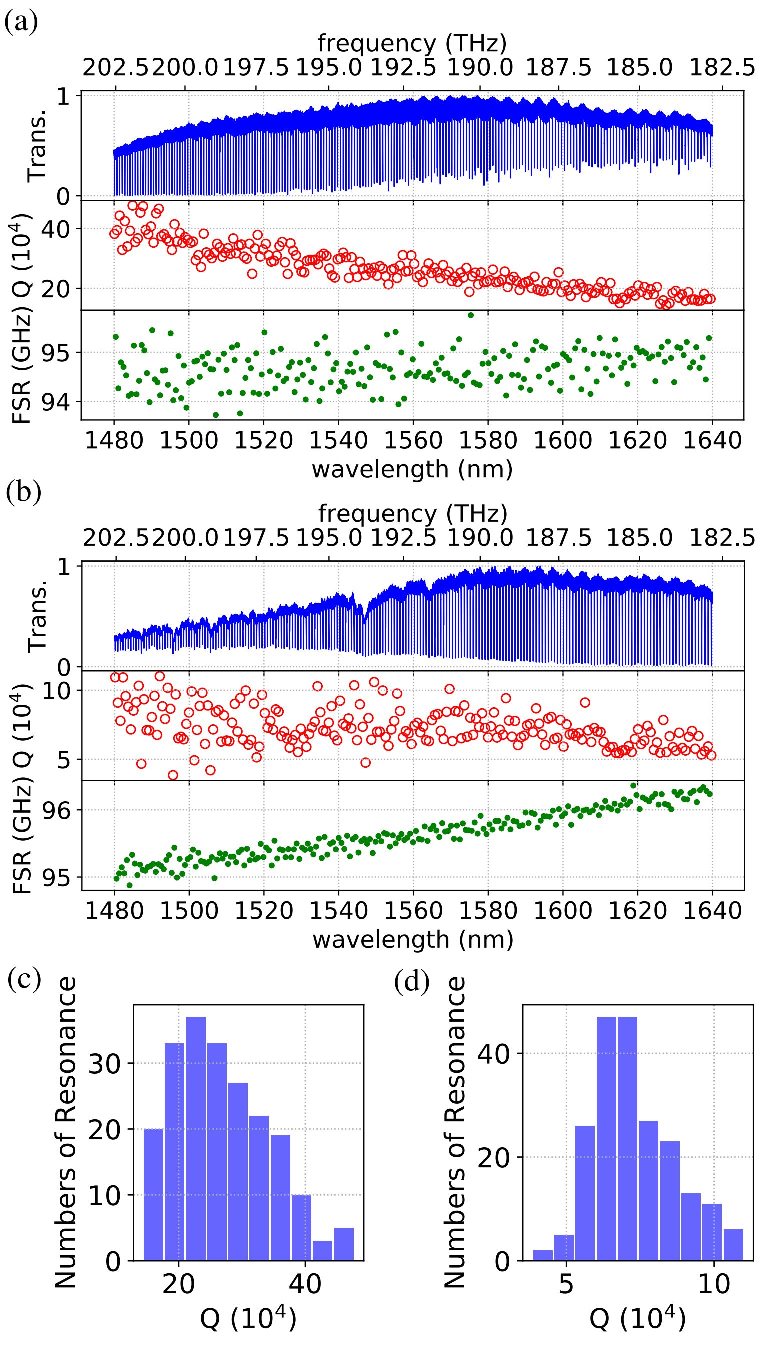

Figure 5.6: **A comparison between identical ring resonator fabricated in Ligentec and NTT-AT technique**.

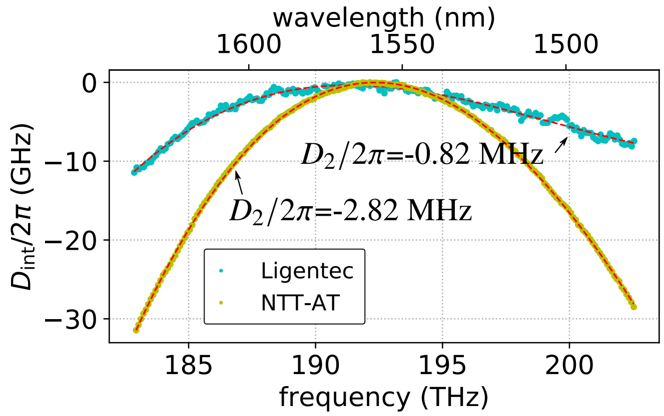

Figure 5.7: Caption

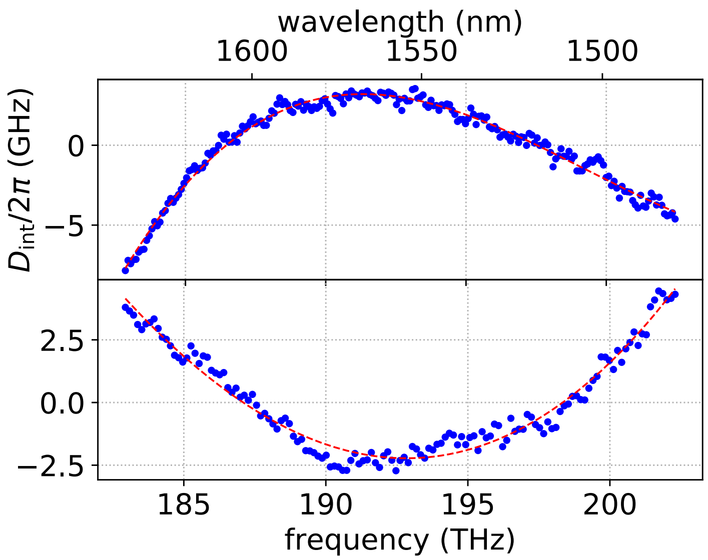

Figure 5.8: Caption

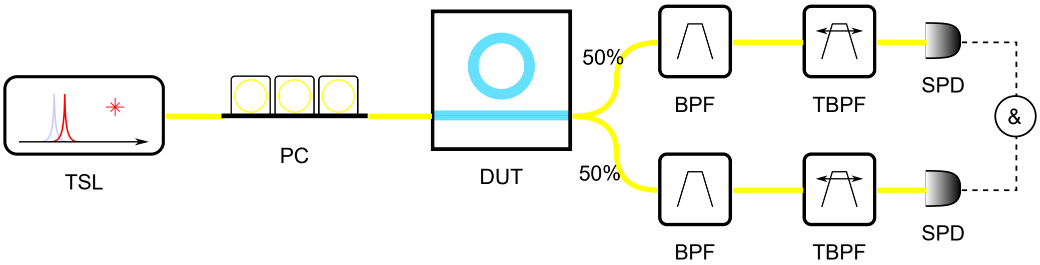

Figure 6.1: Mode-resolvable singular photon pair generation

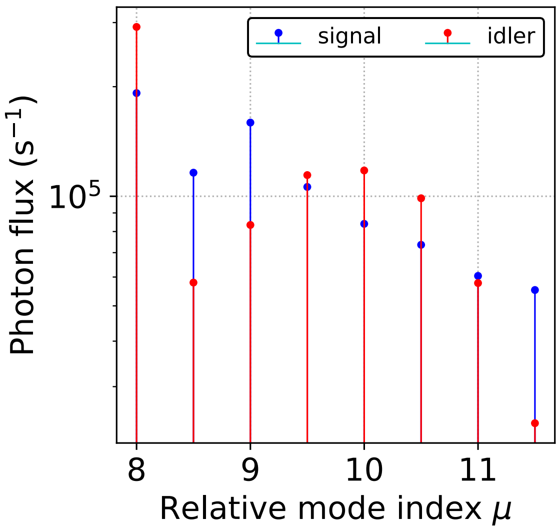

Figure 6.2: **Photon flux at 100 µW of Ligentec group 2 device 1**.

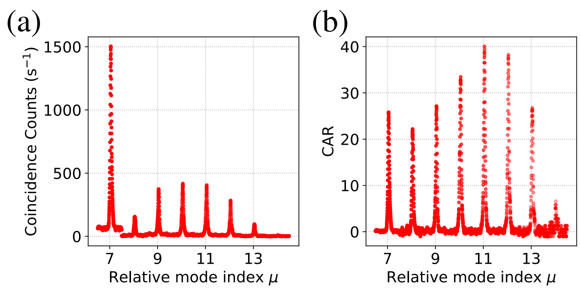

Figure 6.3: **Photon flux at 100 µW of Ligentec group 2 device 1**.

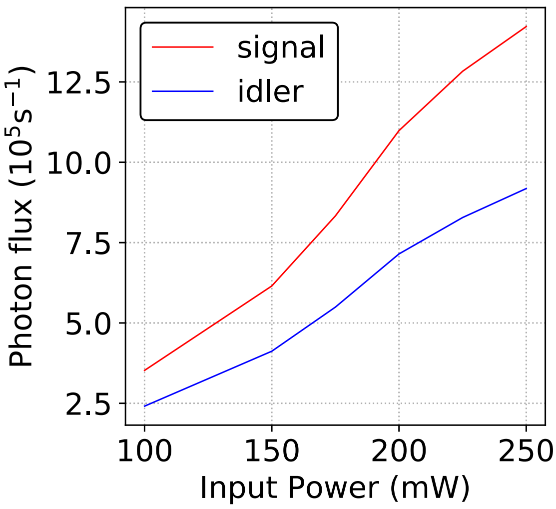

Figure 6.4: .

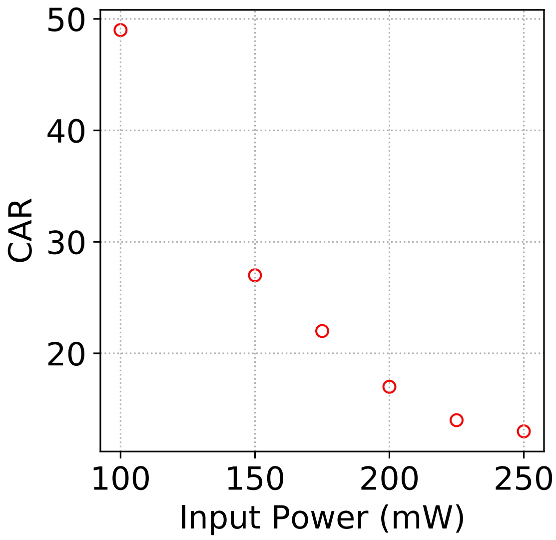

Figure 6.5: .

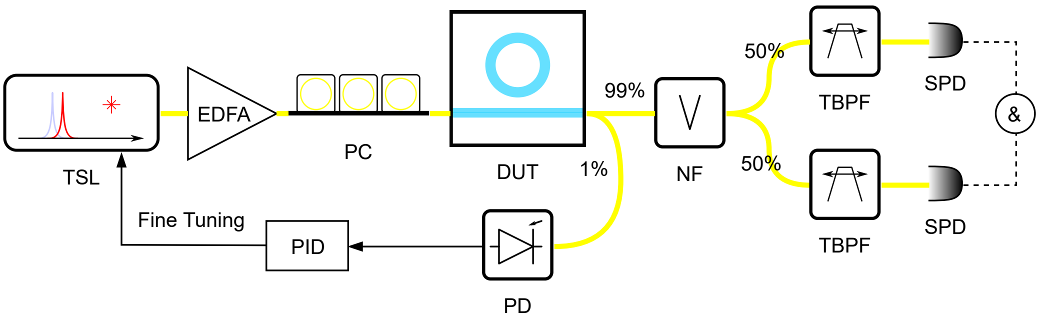

Figure 7.1

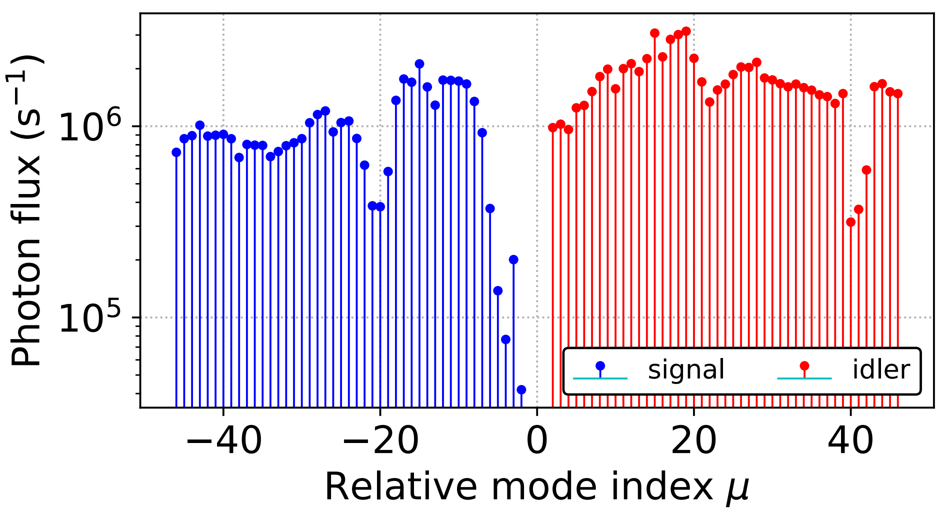

Figure 7.2: **Photon flux at 100 μW of Ligentec group 2 device 1**.

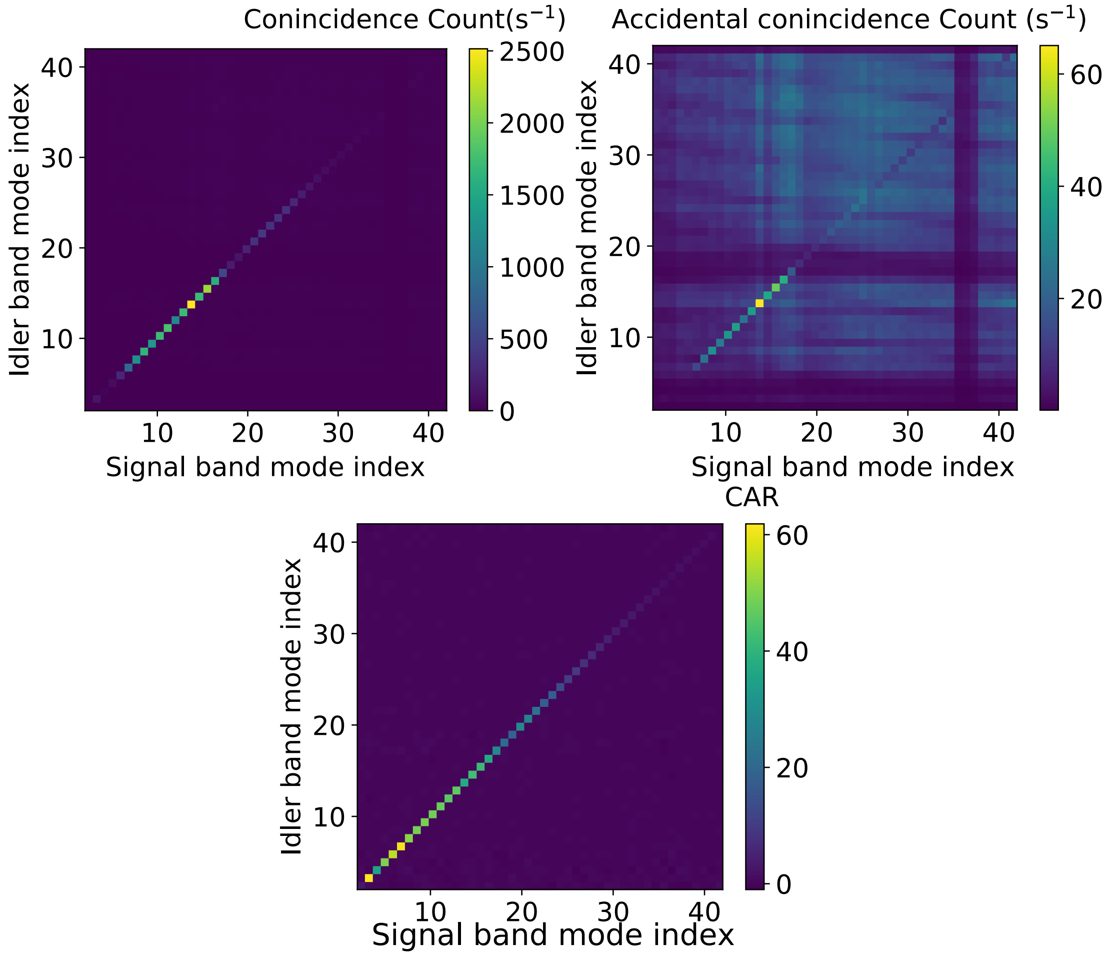
Conincidence Count(s^{-1})
Accidental conincidence Count (s^{-1})
CAR
Idler band mode index
Signal band mode index
2500
2000
1500
1000
500
0
60
40
20
10
20
30
40

Figure 7.3: .

	LP-CVD	PE-CVD	LS-CVD
Facility	-	SAMCO PD-220NL	SMACO PD-100ST
Source	DCS:NH3:N2	SiH_4:NH_3:N2 =6:5:189 sccm	SN-2:N_2 =0.5:30 sccm
Chamber Temp.	750°C-800°C	upper 150°C lower 350°C	upper 150°C lower 180°C
RF Power	-	40 W	30 W
Deposition Rate	-	15 nm/min	23 nm/min

Table 4.1: **Recipes of CVD methods used in this research**. In the case of PE-CVD and LS-CVD, upper electrode and lower electrode are set at different temperature. RF power refers to radio frequency power used to excite the precursor gasses.

	Film Etching Rate (nm/min)	Resist Etching Rate (nm/min)	Selectivity
LP-CVD	19.20	12.76	1.50
PE-CVD	23.48	14.29	1.64
LS-CVD	27.40	2.08	13.17

Table 4.2: **Etching rate and selectivity of ICP process**.

	Ring Radius (μm)	FSR (GHz)	Ring Width (μm)
Group 1	237.28	100	0.8
Group 2	157.95	150	1.7
Group 3	119.90	200	1.5
Group 4	78.55	300	1.7
Group 5	22.95	1000	1.7